International Journal of Plasticity 153 (2022) 103254

Contents lists available at ScienceDirect

International Journal of Plasticity

journal homepage: www.elsevier.com/locate/ijplas

A microstructure-based porous crystal plasticity FE model for additively manufactured Ti-6Al-4V alloys

M. Pinz [a], J.T. Benzing [b], A. Pilchak [c], S. Ghosh [d,*]

[a] Civil and Systems Engineering, Johns Hopkins University, Baltimore, MD 21218, United States of America
[b] Applied Chemicals and Materials Division, National Institute of Standards and Technology, Boulder, CO 80305, United States of America
[c] MRL Materials Resources LLC, Dayton, OH 45440, United States of America
[d] Civil & Systems, Mechanical and Materials Science & Engineering, Johns Hopkins University, Baltimore, MD 21218, United States of America

ARTICLE INFO

Keywords:
Additively manufactured Ti-6Al-4V
Widmanstätten morphology
Statistical representation of 12 α lath variants
Porous crystal plasticity
EBSD scans

ABSTRACT

Building from a foundation of microstructural characterization, mechanical testing, 3D statistically equivalent microstructural volume elements (SEMVEs), and image-based microstructural modeling, this paper develops an effective crystal plasticity model with porosity evolution for additively manufactured Ti-6Al-4V alloys. Their microstructure is characterized by a complex Widmanstätten morphology containing 12 α lath variants. In this paper, the morphology is parametrized by statistically equivalent ellipsoids, enabling a parametric representation of the α laths in the models. An effective crystal plasticity framework with the parametric representation of the α lath morphology is achieved by identifying the crystallographic relationship of the α laths in relation to the parent β grains from which they have nucleated and developing methods to incorporate a statistical representation of HCP α laths in β grains. The constitutive model for β grains statistically accounts for the size, shape, orientation, and crystallography of all 12 α lath variants. An important contribution is the integration of porosity evolution with the crystal plasticity model. The model is calibrated and satisfactorily validated with results from experiments on additively manufactured Ti-6Al-4V alloys with and without heat treatment. The model can yield important insights into the underlying physics of this relatively new class of materials.

1. Introduction

Additive manufacturing (AM) has brought dramatic changes to the manufacturing industry through near-net-shape production of complex, customized parts and structures. Capitalizing on the use of layer-by-layer material addition technology, the AM processes are able to fabricate finished products conforming to 3D computerized designs (Bonatti and Mohr, 2017). Powder-bed AM techniques, such as electron beam melting (EBM) and laser powder bed fusion (LPBF), involving layer-wise melting of powder have shown great promise in manufacturing metallic components, e.g. of titanium and aluminum alloys (Knezevic et al., 2021; Chen and Li, 2019). Despite the significant promise, the qualification and certification of AM processed materials are often impeded by inconsistencies in the overall mechanical behavior and extreme properties (Khairallah et al., 2020; Voisin et al., 2018; Francois et al., 2017), commonly attributed to subtle, yet characteristic variations in the microstructural morphology like grain size, crystallographic texture, and defect structures (Boyce et al., 2017; Salzbrenner et al., 2017; Muhammad et al., 2021).

Among various metallic materials, additively manufactured Ti-6Al-4V promises to be a transformational material in high-performance, mission-critical components due to its impressive strength and a large design envelope (Liu and Shin, 2019). These

* Corresponding author.
E-mail address: sghosh20@jhu.edu (S. Ghosh).

https://doi.org/10.1016/j.ijplas.2022.103254
Received 2 December 2021; Received in revised form 8 February 2022
Available online 3 March 2022

materials exhibit a complex, Widmanstätten or basket-weave microstructure (Gil et al., 2001), with over 98% hexagonal close-packed (HCP) α phase that forms due to the high cooling rates in the AM process. Following solidification after energy injection in the EBM process, the material initially exists in the body-centered cubic (BCC) β phase. However, upon the cooling below 950 °C, the transus temperature of Ti-6Al-4V, α laths begin to precipitate and form individual α colonies with one of 12 unique Burgers relationships with respect to the parent β grain (Kobryn and Semiatin, 2001; Humbert and Gey, 2002). The highly localized heating source in the electron beam and laser processes (Lin et al., 2019; Yang et al., 2016) results in a far more rapid cooling rate of the molten material than for other bulk processes. With the high cooling rate, more nucleation sites are formed resulting in smaller and more intricate α laths. These microstructures also contain defects intrinsic to the AM processes in the form of void and porosity distribution, due to either lack of fusion or key-holing events (Beretta and Romano, 2017; Pegues et al., 2019; Gong et al., 2014). An understanding of the interplay between the complex Widmanstätten microstructure of Ti-6Al-4V and the porosity defects (Montalbano et al., 2021; Qiu et al., 2013; Book and Sangid, 2016; Watring et al., 2021) is important for capturing the overall mechanical and failure properties of these additively manufactured materials. Robust micromechanical models that can effectively couple the detailed effects of these aspects of the microstructure are of high relevance in the effective design and manufacture of these materials.

There is an extensive literature on image-based modeling approaches for dual-phase α/β Ti-6Al-4V (Liu et al., 2020; Kasemer et al., 2017; Mayeur and McDowell, 2007; Mayeur et al., 2008; Chatterjee et al., 2018; Hu et al., 2020; Thomas et al., 2012; Feng et al., 2020). For example, physics-based micromechanical models of dwell fatigue due to load shedding and plastic strain localization in temperature and rate-sensitive materials have been proposed for Ti alloys in Zheng et al. (2018), Xu et al. (2020), Anahid et al. (2011), Ozturk et al. (2017). However, there is a paucity of modeling-based studies on Widmanstätten microstructures of AM-processed Ti-6Al-4V materials (Seifi et al., 2016). This in part is due to the difficulty of statistical characterization of individual α laths, interlocked in a basket-weave pattern as shown in Fig. 1. A few studies with this material include crystal plasticity modeling with grain-level residual stresses (Kapoor et al., 2018) and crystal plasticity model-based prediction of tensile properties (Azhari et al., 2022). Image-based micromechanical models need the creation of virtual microstructures from experimental electron backscattered diffraction (EBSD) and/or scanning electron microscopy (SEM) scans, e.g. the statistically equivalent microstructural volume elements (SEMVEs) (Pinz et al., 2018; Bagri et al., 2018). The intricate, interwoven Widmanstätten microstructures formed by the AM processes are difficult to characterize without high-resolution 3D scans, such as dual-beam focused ion beam (FIB)-based EBSD or SEM scans (Echlin et al., 2012). 2D surface scans lack the detailed information needed for creating representative high-resolution 3D virtual microstructures. Alternative methods, such as the phase-field approach of microstructure evolution from β to α phase (Shi and Wang, 2013; Shi et al., 2015; Zhang et al., 2021; Radhakrishnan et al., 2016), while promising, are computationally expensive.

The present study is aimed at the development of a micromechanical model for deformation analysis of AM-based Ti-6Al-4V with Widmanstätten microstructures. The grain microstructure contains up to 12 unique HCP α laths with $\geq$98% volume fraction, each with its own crystallographic orientation and slip systems. Explicit representation of each of the 12 α lath variants in FE models of the microstructural grains is computationally prohibitive due to their extremely small scale. It will require an enormously large number of elements to represent individual phases. In lieu of explicit representation, the α laths are represented by a statistical representation of the morphology (e.g. volume fraction, size, and shape) and crystallography of the α laths in the parent grain, matching distributions observed in the EBSD scans. Statistically equivalent microstructural volume elements or SEMVEs are generated by equating the statistics of various morphological and crystallographic descriptors of the EBSD scans of the microstructure with those for the model (Pinz et al., 2018; Bagri et al., 2018). The SEMVE is a microstructural domain for which statistical distribution functions of morphological parameters converge to those of the experimental microstructure. Unlike representative volume elements (RVEs) that are conventionally subjected to periodic boundary conditions, boundary conditions on the SEMVE resemble the experimental loading conditions for generating overall response functions of the specimen. For the problems considered in this study, the use of RVEs with periodic boundary conditions is deemed inappropriate due to the localization (non-periodic) deformation patterns observed in the experimental specimen.

The crystallographic orientations of the α laths are functions of the crystallography of the parent β grain. In this approach, the effects of each of the 12 variants are incorporated into a constitutive framework of an equivalent crystal. This concept follows the equivalent crystal model that has been developed in Deka et al. (2006) for transformed β colonies in the Ti-6242 alloy microstructure, consisting of alternating parallel α and β laths. The equivalent crystal consists of an assemblage of 30 HCP and 48 BCC slip systems that are oriented in accordance with the Burgers relation. Assuming a Taylor model, the stress tensor in the equivalent crystal is determined using the rule of mixtures, where a weighted averaging of the α and β phase stresses is conducted, with phase volume fractions as weights. In the present study, the equivalent grain is developed for the 12 unique α laths and incorporated into an effective constitutive relation. Voids in the model microstructure are assumed to manifest in the form of porosity distributions. The effect of porosity distributions in the equivalent grain is accommodated through a porous crystal plasticity constitutive model that has been developed in Yang and Ghosh (2022) to capture the effect of evolution of porosity (void volume fraction), crystallographic orientation, void growth, stress triaxiality, and Lode parameters. This porosity evolution and associated crystal plasticity model in Yang and Ghosh (2022) is adopted in this work for simulating Widmanstätten microstructures in additively manufactured Ti-6Al-4V. This combination of the microstructure and defect representation provides a strong and viable computational model to interrogate and develop microstructure-response relations for this additively manufactured Ti alloy.

This paper begins with a description of the material, mechanical testing regimens, and the image acquisition methods used for microstructure statistics gathering in Section 2. Section 3 discusses the cleanup procedures for the microstructural images, the methodologies for determining the parent β grains from images containing only α laths, the construction of 3D statistically equivalent microstructural volume element of parent β microstructures, as well as the generation of statistically equivalent α phase inputs for the

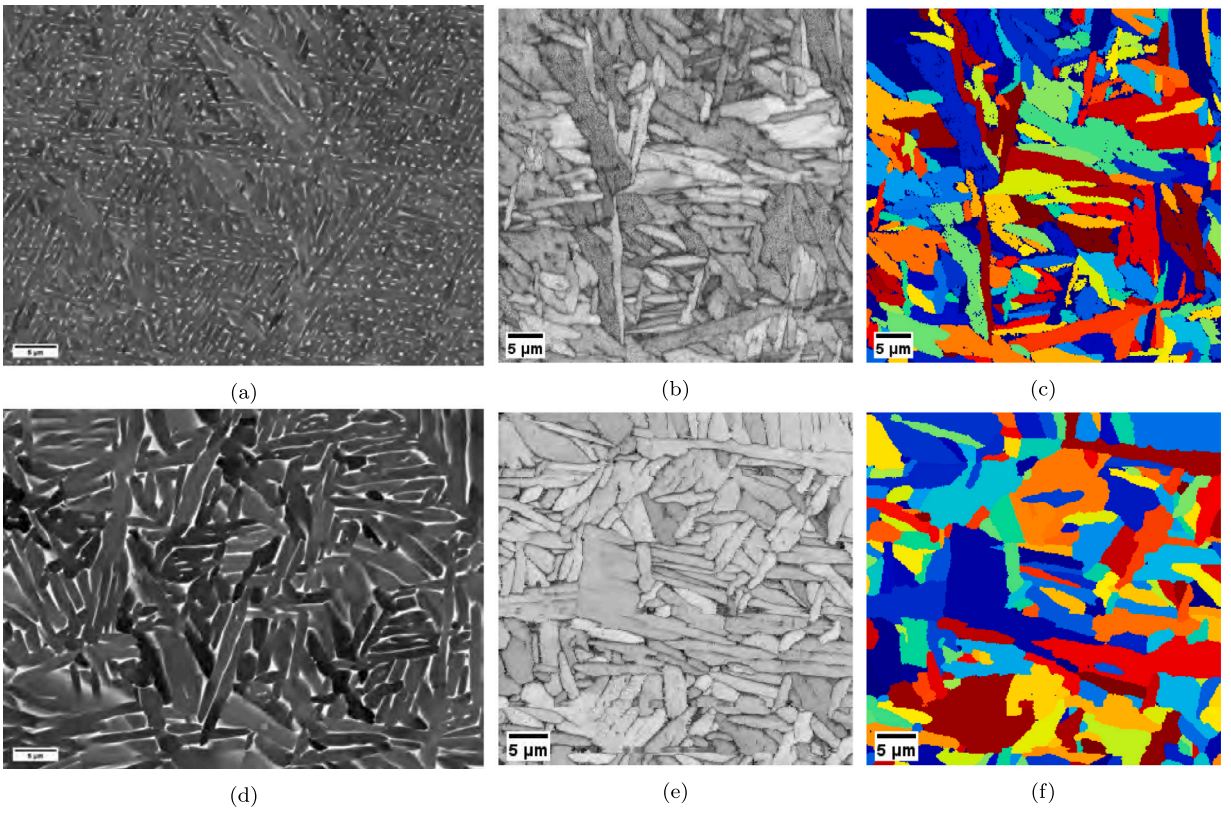

Fig. 1. (a) Backscattered electron (BSE) image, (b) image quality map of electron backscattered diffraction (EBSD) scan, and (c) feature ID map of EBSD scan of as-built additively manufactured Ti-6Al-4V microstructure, (a unique color is used represent each individual feature, corresponding to α grains); (d) BSE image, (e) image quality map of EBSD scan, and (f) feature ID map of EBSD scan of a HIP-treated Ti-6Al-4V microstructure (a unique color is used represent each individual feature, corresponding to α grains). (For interpretation of the references to color in this figure legend, the reader is referred to the web version of this article.)

effective crystal plasticity model. Section 4 provides a comprehensive overview of the porous crystal plasticity formulation derived for the equivalent crystal model. Section 5 describes the calibration of the constitutive parameters and the subsequent validation with results from mechanical tests. This is supplemented with additional validation for a hot isostatic pressing (HIP)-treated material that contains minimal porosity. Finally, the paper concludes with a summary in Section 7

2. Summary of the material, manufacturing process, and testing

2.1. Additively manufactured Ti-6Al-4V alloy

Additively manufactured Ti-6Al-4V is nominally an α/β Ti alloy, with small amounts of vanadium, aluminum, and other elements. The weight fractions of the experimental alloy in this work are 5.82%Al, 4%V, 0.2%Fe, 0.1%O, with trace amounts of C, H, and N, the balance being Ti. The EBSD scans of the Ti-6Al-4V microstructure contain $\geq 98\%$ α phase by area, demonstrating that the deformation mechanisms are dominated by dislocation glide on HCP slip systems. Accordingly, the model accounts for deformation of the α phase in the Widmanstätten microstructure that is characterized by interlocking plates, forming α lamellae. The α laths precipitate out of the β phase, as the material cools below the β transus temperature. The α laths are approximately ellipsoidal in nature and are related to the parent β grain via a Burgers relationship $(0001)_\alpha \parallel (101)_\beta$ and $[11\bar{2}0]_\alpha \parallel [\bar{1}11]_\beta$, discussed in Burgers (1934). The crystallographic rotation matrix D that describes the rotation from a vector in the β crystal coordinate system to the α phase coordinate system is given in Humbert et al. (1995) as:

$$D = \begin{bmatrix} -\frac{1}{2}\left(1+\frac{1}{\sqrt{6}}\right) & \frac{1}{2}\left(\frac{1}{\sqrt{3}}-\frac{1}{\sqrt{2}}\right) & \frac{1}{\sqrt{2}} \\ \frac{1}{2}\left(1+\frac{1}{\sqrt{6}}\right) & -\frac{1}{2}\left(\frac{1}{\sqrt{3}}-\frac{1}{\sqrt{2}}\right) & \frac{1}{\sqrt{2}} \\ -\frac{1}{2}\left(1-\frac{2}{\sqrt{6}}\right) & \frac{1}{2}\left(\frac{1}{\sqrt{3}}+\frac{1}{\sqrt{2}}\right) & 0 \end{bmatrix} \tag{1}$$

Table 1
Crystallographic relationship of the 12 variants to the parent β grain, defined by rotation matrices and quaternions.

Variant number i	Rotation matrix S_i^β	Quaternions	Burgers relationship
1	$\begin{bmatrix} 1 & & \\ & 1 & \\ & & 1 \end{bmatrix}$	[1, 0, 0, 0]	$(101)\|\|(0001)$, $[\bar{1}11]\|\|[11\bar{2}0]$
2	$\begin{bmatrix} 1 & & \\ & -1 & \\ & & -1 \end{bmatrix}$	[0, −1 ,0, 0]	$(\bar{1}01)\|\|(0001)$, $[111]\|\|[11\bar{2}0]$
3	$\begin{bmatrix} & & 1 \\ 1 & & \\ & 1 & \end{bmatrix}$	[0.5, 0.5, 0.5, 0.5]	$(011)\|\|(0001)$, $[11\bar{1}]\|\|[11\bar{2}0]$
4	$\begin{bmatrix} & & -1 \\ -1 & & \\ & 1 & \end{bmatrix}$	[0.5, 0.5, −0.5, −0.5]	$(01\bar{1})\|\|(0001)$, $[\bar{1}11]\|\|[11\bar{2}0]$
5	$\begin{bmatrix} & -1 & \\ & & -1 \\ 1 & & \end{bmatrix}$	[0.5, 0.5, −0.5, 0.5]	$(1\bar{1}0)\|\|(0001)$, $[11\bar{1}]\|\|[11\bar{2}0]$
6	$\begin{bmatrix} & -1 & \\ & & 1 \\ -1 & & \end{bmatrix}$	[0.5, −0.5, 0.5, 0.5]	$(110)\|\|(0001)$, $[\bar{1}11]\|\|[11\bar{2}0]$
7	$\begin{bmatrix} -1 & & \\ & 1 & \\ & & -1 \end{bmatrix}$	[0, 0, −1, 0]	$(101)\|\|(0001)$, $[11\bar{1}]\|\|[11\bar{2}0]$
8	$\begin{bmatrix} -1 & & \\ & -1 & \\ & & 1 \end{bmatrix}$	[0, 0, 0, −1]	$(\bar{1}01)\|\|(0001)$, $[1\bar{1}1]\|\|[11\bar{2}0]$
9	$\begin{bmatrix} & & -1 \\ 1 & & \\ & -1 & \end{bmatrix}$	[0.5, −0.5, −0.5, 0.5]	$(011)\|\|(0001)$, $[1\bar{1}1]\|\|[11\bar{2}0]$
10	$\begin{bmatrix} & & 1 \\ -1 & & \\ & -1 & \end{bmatrix}$	[0.5, −0.5, 0.5, −0.5]	$(01\bar{1})\|\|(0001)$, $[111]\|\|[11\bar{2}0]$
11	$\begin{bmatrix} & 1 & \\ & & -1 \\ -1 & & \end{bmatrix}$	[0.5, 0.5, 0.5, −0.5]	$(1\bar{1}0)\|\|(0001)$, $[111]\|\|[11\bar{2}0]$
12	$\begin{bmatrix} & 1 & \\ & & 1 \\ 1 & & \end{bmatrix}$	[0.5, −0.5, −0.5, −0.5]	$(110)\|\|(0001)$, $[1\bar{1}1]\|\|[11\bar{2}0]$

However, due to the symmetry of the BCC crystal, there are 12 symmetry operators represented by a matrix S_i^β, which can generate unique variants (Shi and Wang, 2013; Humbert et al., 1995). Defining the rotation matrix from the reference coordinates to the crystallographic coordinates of the parent β grain as G, the rotation matrix P^i from the reference orientation to the ith variant's α crystallographic orientation is expressed as:

$$P^i = DS_i^\beta G \tag{2}$$

A derivation of the relationship between α and parent β phases can be found in Humbert et al. (1995). An exhaustive list of the symmetries, resulting in varying S_i^β is provided in Table 1.

Each of the 12 variants represents a unique way to attach the HCP lattice onto a given BCC orientation. Table 1 provides the rotations of these symmetries that give rise to the variants in both the matrix forms and in quaternions. Quaternions, detailed in Section 3.2, are an alternate approach to representing rotations. The table also shows the unique Burgers relationship between the α and the β phases. A similar table without the quaternion representation is given in Shi and Wang (2013).

2.2. Material build parameters in the electron beam melting process

The Ti-6Al-4V specimens are fabricated using electron beam melting powder-bed fusion (EBM-PBF) in an Arcam A1 machine (software version 3.2.132),[1] schematically shown in Fig. 2. The accelerating voltage is 60 kV, and the layer thickness is 50 μm. The standard Arcam Ti-6Al-4V gas-atomized powder used, has a specified particle size range of approximately 40 μm to 100 μm, and an

[1] Certain commercial software, equipment, instruments or materials are identified in this paper in order to specify the experimental procedure adequately. Such identification is not intended to imply recommendation or endorsement by the National Institute of Standards and Technology, nor is it intended to imply that the equipment or materials identified are necessarily the best available for the purpose.

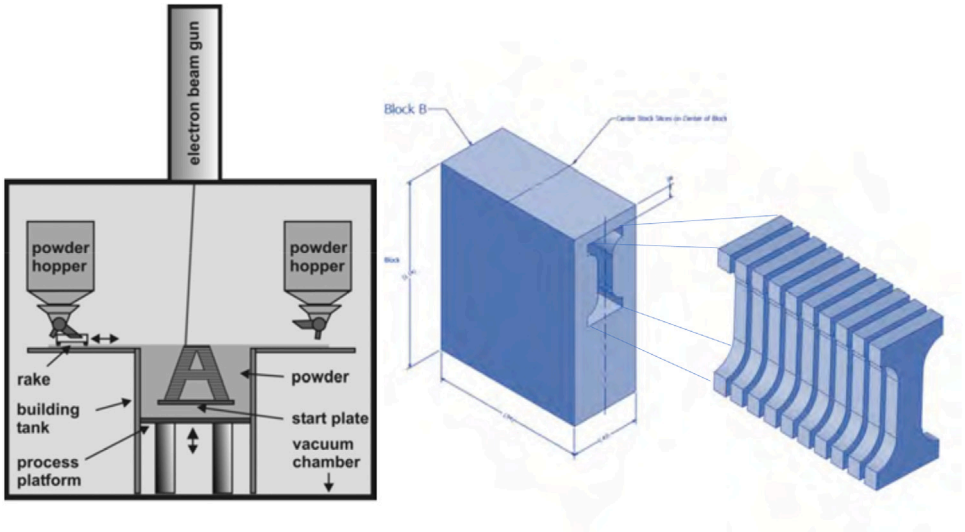

Fig. 2. Overview of the powder-bed fusion build process with example build coupon and extraction of testing samples.

average diameter of approximately 70 μm. Parts are grouped into a single melt model such that the EBM scan length is approximately 70 mm in each of the in-plane directions.

One subgroup of the samples is subjected to a hot isostatic pressing (HIP) treatment below the β transus at 900 °C for two hours in an inert Ar environment at a pressure of 100 MPa. Heating and cooling rates are carried out at 12 °C/min, a process that is primarily used to eliminate porosity in the material due to the AM process. This has the added effect of allowing the α laths to slowly coarsen over the course of the treatment, similar to the Ostwald ripening process.

2.3. Tension testing

Ten tensile specimens are excised from the upper half of selected Ti-6Al-4V components, using electrical discharge machining (EDM), for three material-load direction pairs. The material-load pairs include:

- **Set 1**: Ten samples of as-built material without heat treatment, loaded along the build direction;
- **Set 2**: Ten samples of as-built material without heat treatment, loaded perpendicular to the build direction.
- **Set 3**: Ten samples of HIP-treated material loaded along the build direction;

The tensile specimens with 12.7 mm total length, 1.27 mm thickness, 2.54 mm gauge width, and a 3 mm gauge length set by an extensometer, are deformed at a strain rate of 10^{-3} s^{-1} in uniaxial tension. The linear portion of the stress–strain curve is fit in accordance with ASTM E3076-18 (ASTM, 2011a) to calculate the Young's modulus. The other tensile properties, e.g. yield strength, ultimate strength, uniform elongation, and elongation at fracture, are found according to ASTM E8-16a (ASTM, 2011b) and have been previously reported for this particular EBM-PBF build in Benzing et al. (2019). An analysis of variance is completed with InStat software (Bailey and Stern, 2021) and used to test the null hypotheses that the tensile properties are equal across material conditions with a statistical significance of $p \leq 0.01$.

2.4. Defect characterization

Samples of each material condition are analyzed for internal porosity with an X-ray computed tomography (CT) machine (Zeiss Xradia) with the following parameters: 160 kV, 10 W, 1 μm voxel size. The volume-averaged porosity is found to be 0.1% for the as-built conditions, and negligible for the HIP-treated samples.

2.5. Microstructural characterization with EBSD scans

Samples from each material condition are sectioned from the same build height (Z = 20 mm), ground with SiC paper (400 grit through 1200 grit), polished with a suspension of 1 μm diamond particles and finished with a vibratory polish using 50 nm colloidal silica. Backscattered electron images, as shown in Fig. 1(a, d), are recorded using a Zeiss Gemini field-emission scanning electron microscope (FE-SEM): 20 kV, 60 μm aperture, high current mode, and an 8 mm working distance. Six small-area electron backscatter diffraction (EBSD) scans in Fig. 1(b, c, e, f) are performed for each material condition using a Zeiss Leo FE-SEM: 20 kV, 120 μm aperture, 7.8 nA current, and a 19 mm working distance. For the purposes of measuring α lath thickness and phase fraction,

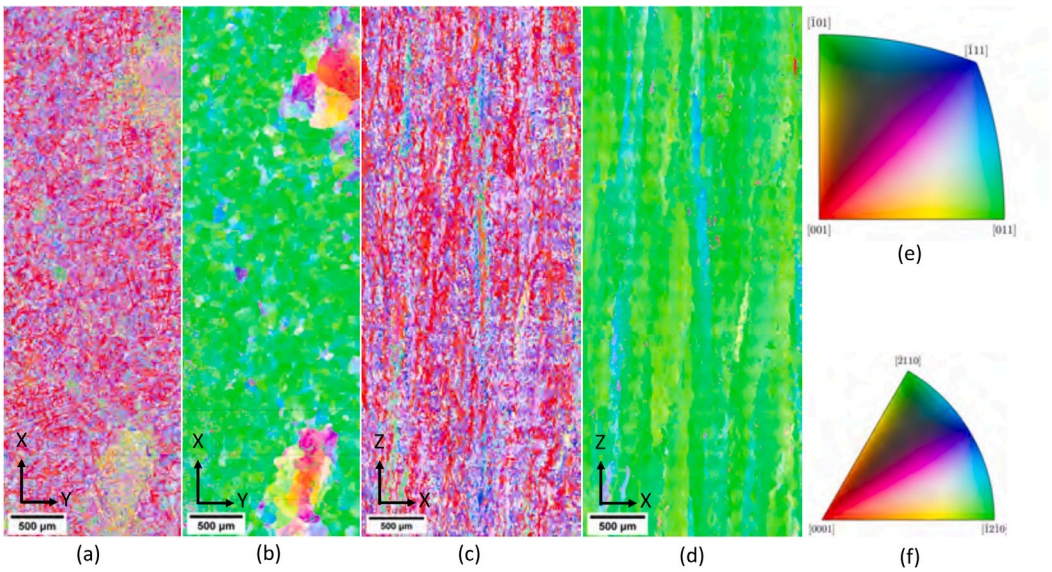

Fig. 3. (a) As-scanned XY EBSD map of α laths in the AM-based Ti-6Al-4V microstructure, (b) reconstructed β XY EBSD map, (c) as-scanned XZ EBSD map of α laths in the AM-based Ti-6Al-4V microstructure, (d) reconstructed β XZ EBSD map, (e) IPF key for the reconstructed β EBSD maps in figures (b, d), (f) IPF key for the as-scanned EBSD maps in figures (a, c). (For interpretation of the references to color in this figure legend, the reader is referred to the web version of this article.)

the EBSD step size is 0.150 μm and the field of view is 50 μm × 50 μm. Multi-tile large-area EBSD scans are performed for each material condition and encompass at least 10 mm^2 in area. The measurements are performed with a Zeiss Leo FE-SEM: 20 kV, 120 μm aperture, 7.8 nA current, and a 19 mm working distance. A step size of 1 μm is used to capture global texture in each 450 μm × 450 μm tile.

3. Microstructure characterization and generation of Statistically Equivalent Microstructural Volume Elements (SEMVEs)

Micromechanical simulations of additively manufactured Ti-6Al-4V alloys are conducted on SEMVEs (Pinz et al., 2018; Bagri et al., 2018) generated by equating the statistics of various morphological and crystallographic descriptors of EBSD scans of the microstructure. The statistics extracted from the experimental micrographs necessarily correspond to the thermodynamic processes in the microstructure generation process. The aim of constructing statistical instantiations of microstructural descriptors is to describe the natural variation within the observed microstructure and to incorporate this stochasticity into the constitutive model. The following process of generating SEMVEs is tailored to provide an unbiased estimation of the microstructural statistics, hewing as closely as possible to the observed statistical distributions.

3.1. Image processing and statistical analysis of α laths

An automated procedure is established for cleanup and segmentation to acquire the statistics of the size, shape, orientation, and crystallography of α laths in the Ti-6Al-4V microstructure. Large-area images with lower resolution and high-resolution small-area images are sampled for microstructural characterization and statistical analysis. After stitching together, the large-area images containing 0.4 μm pixel sizes, have overall dimensions of 1042 μm by 3116 μm for the XY EBSD scan, and 1996 μm by 4822 μm for the XZ EBSD scan. These α lath scans are shown in Figs. 3(a, c), and the corresponding IPF color keys are shown in Fig. 3(f). These images are primarily used for determining the relative volume fraction of variants, as well as the morphology of the parent β grains. More detailed small-area scans, with a pixel size of 0.15 μm, are used for characterizing the α lath morphology.

The EBSD scans are all imported into the DREAM.3D suite (Groeber and Jackson, 2014), and the following steps are applied for consistency.

1. A bad data filter is applied to remove any pixel with a confidence index ≤ 0.1, followed by a *fill bad data* approach to use nearby pixel information to replace the removed data;
2. Individual grains are next segmented with a 1° misorientation tolerance;
3. Any segmented feature containing fewer than 50 pixels is removed from both the small and large area images, and the feature IDs are replaced via a burn algorithm.
4. The best-fit ellipse and mean crystallographic orientation are calculated for every segmented grain, to calculate the grain aspect ratio and orientation.

The thickness distributions of the α laths are determined from the thickness of 60 different α laths in the ensemble. The α lath size has a significant length-scale effect in the crystal plasticity model.

3.2. Construction of parent beta grains and variant identification

The reconstruction methodology is based on the methods described in Glavicic et al. (2003a,b). In consideration of rotational symmetries of the parent β and child α phase, a particular β phase orientation can give rise to 12 unique α variants, as identified in Table 1. Among these, however only five are unique crystallographic misorientations, which can be used to reconstruct the β phase. The quaternion representation of orientation space is employed in this development, where an arbitrary orientation is represented with a unit quaternion (Kocks et al., 1998) as:

$$\bar{\mathbf{q}} = (q_0, \mathbf{q}) = \{q_0, q_1, q_2, q_3\} \quad \text{with the constraint} \quad (q_0)^2 + (q_1)^2 + (q_2)^2 + (q_3)^2 = 1$$

Here q_0 and $\mathbf{q} = (q_1, q_2, q_3)$ represent the scalar and vector parts of the quaternion, respectively.

The algorithm for generating parent β grains from the image of a child α laths begins by aggregating the pixel-level orientation data into α laths defined in the previous section. A burn algorithm, which locates edge-connected pixels containing crystallographic misorientations less than a user-specified tolerance, is executed. The misorientation $\Delta\bar{\mathbf{q}}^{ab}$ between two quaternions $\bar{\mathbf{q}}^a$ and $\bar{\mathbf{q}}^b$ is the quaternion product of the inverse of $\bar{\mathbf{q}}^b$ and $\bar{\mathbf{q}}^a$, defined as:

$$\Delta\bar{\mathbf{q}}^{ab} = \Delta(\bar{\mathbf{q}}^a, \bar{\mathbf{q}}^b) = (\bar{\mathbf{q}}^a)^{-1} \cdot \bar{\mathbf{q}}^b = (q_0^a q_0^b - \mathbf{q}^a \cdot \mathbf{q}^b, q_0^a \mathbf{q}^b + q_0^b \mathbf{q}^a + \mathbf{q}^a \times \mathbf{q}^b) \tag{3}$$

This misorientation is related to a rotation angle ω that is expressed through the relation $q_0 = cos(\frac{\omega}{2})$, whereas the rotation axis $\mathbf{n}$ is obtained from the relation $\mathbf{q} = \mathbf{n} sin\left(\frac{\omega}{2}\right)$. The average orientation is calculated from this data by ensuring that all pixels belonging to a grain i are in the fundamental zone, defined as the minimum set of orientations such that all crystallographic orientations can uniquely map to it (MTEX, 2021). The conventions used in this paper are the same as those employed in the open-source software package MTEX (Krakow et al., 2017).

To acquire this, the product of the measured quaternion $\bar{\mathbf{q}}^i_{measured}$ with the rotational symmetry operators S_k^{HCP} is taken for HCP crystals, such that $\bar{\mathbf{q}}^i = \bar{\mathbf{q}}^i_{measured}[S_k^{HCP}]$ for $k = 1...12$. A single symmetry k^* is chosen from the set $k = 1 \dots 12$, such that $\bar{\mathbf{q}}^i$ is in the fundamental zone. With all orientations in the fundamental zone identified as being in the same grain, the average orientation can be approximated as the arithmetic mean of the quaternions normalized by their respective vector norm (Cho et al., 2005) as:

$$\langle \bar{\mathbf{q}} \rangle = \frac{1}{N} \sum_{n=1}^{N} \frac{\bar{\mathbf{q}}^n}{\|\bar{\mathbf{q}}^n\|} \tag{4}$$

Unique α laths are identified from clusters of pixels, following steps delineated in Section 3.1. Subsequently, an algorithm is executed to loop over segmented α laths that are not yet assigned to a contiguous β region, using the following steps.

- For a selected ith α lath, a list of all contiguous α laths with a shared boundary is constructed.
- All possible misorientations between the ith α lath and the jth neighbor are computed from the relation $\Delta\bar{\mathbf{q}}_k^{ij} = S_k^{HCP} \Delta\bar{\mathbf{q}}^{ij} S_k^{HCP}$. Symmetry operators are applied on both sides of this misorientation.
- As before, the quaternion in the fundamental zone is identified and the misorientation between the ith α lath and jth neighbor is recorded as $\Delta\bar{\mathbf{q}}_{k^*}^{ij}$.
- The misorientation between the ith and jth α laths $\Delta\bar{\mathbf{q}}_{k^*}^{ij}$, and the set of the six crystallographically allowable misorientations between α laths from the same parent β grain $\bar{\mathbf{q}}_l^{BOR}$ in Table 2 are computed as $\Delta(\bar{\mathbf{q}}_l^{BOR}, \Delta\bar{\mathbf{q}}_{k^*}^{ij})$.
- If the smallest of these resultant misorientations is less than a user-specified tolerance (3° in this paper), i.e.

$$\min_l(|\Delta(\bar{\mathbf{q}}_l^{BOR}, \Delta\bar{\mathbf{q}}_{k^*}^{ij})|) < tolerance, \quad \text{where } |\cdots| \text{ represents only the scalar part of the quaternion}$$

  then the two variants are assumed to have been inherited from the same parent β grain, and are temporarily marked as belonging to the same β region.

It should be noted that in a few special cases, α variants within different prior β grains can share one of these crystallographic misorientations through some underlying crystallographic relationship in the parent β grains, such as sharing a common $\langle 110 \rangle$ axis (Bhattacharyya et al., 2003). The present method relies on tight crystallographic tolerances, by driving the minimum tolerance angle on the initial segmentation of pixels-to-grains down as far as possible. An alternate robust method has been recently proposed in Zaitzeff et al. (2021).

At least 4 unique variants are required to uniquely identify the orientation of the parent β orientation from the observed α lath crystallography (Cayron, 2007). If there are fewer than 4 unique α laths belonging to the same β grain, then the β orientation is not guaranteed to be calculable. Hence, if clusters of α laths belonging to the same parent β grain contain more than 4 unique variants, then this cluster has a unique solution to identifying the parent β grain orientation. However, if there are fewer than 4 unique variants, the cluster is disbanded, and the loop is passed to the next iteration.

Following identification, the orientations of the contiguous β grains are computed by first calculating trial orientations comprised of all 6 possible parent β orientations for each α lath within an identified β region. The trial β orientations are calculated by the formula $T_l = \bar{\mathbf{q}}^{D^{-1}} S_l^\alpha \bar{\mathbf{q}}^\alpha$, where S_l^α is a special subset of six of the hexagonal rotational symmetry elements described in Glavicic

Table 2
List of all possible quaternion misorientations between two α variants inherited from the same prior β grain, $\bar{\mathbf{q}}_l^{BOR}$.

Unique orientation ID	q_0	q_1	q_2	q_3
1	1	0	0	0
2	0.9958	0	0	−0.0918
3	0.7071	0.2959	−0.6422	0
4	0.8514	−0.5000	0	−0.1582
5	0.8624	−0.4979	0.0459	−0.0795
6	0.8660	0.2500	0.4330	0

et al. (2003a), $\bar{\mathbf{q}}^{D^{-1}} = \{0.5406,\ 0.7046,\ -0.0800,\ 0.4558\}$ is the inverse of Eq. (1) in quaternion form, and $\bar{\mathbf{q}}^{\alpha}$ is the orientation of the α lath. A list of all trial β orientations is constructed as β_{ml}, where m ranges from 1 to the number of α laths in the previously identified β region, and l represents each of the 6 possible trial β orientations. From this list β_{ml}, the orientation β is calculated by solving an optimization problem, delineated as:

$$\boldsymbol{\beta} = \min_{\boldsymbol{\beta}} \sum_{m=1}^{n_{Neighbors}} |\Delta(\boldsymbol{\beta}, \beta_{ml})|^2 I_{ml} \quad S.T. \quad I_{ml} \in \mathbb{Z}[0,1] \quad , \quad \sum_{l=1}^{6} I_{ml} = 1 \quad \forall\, m \tag{5}$$

where $|\Delta(\boldsymbol{\beta}, \beta_{ml})|$ represents only the scalar portion of the quaternion, and I_{ml} is an indicator function that contains only one positive value for each mth entry. The resultant $\boldsymbol{\beta}$ is the orientation that has the minimum misorientation between each of the trial β orientations. The pseudo-code for generating the parent β grain from the α laths is given in Appendix A. An exit criteria may be incorporated to avoid the rare possibility for this algorithm to end in an infinite loop if not all grains can be assigned.

Figs. 3(b, d) show the reconstructed β section maps, and the corresponding IPF color keys are shown in Fig. 3(e). The different orientation between the as-scanned EBSD and reconstructed suggests that there is a strong preference for the ⟨011⟩ direction of the prior β grains, and that any of the 12 unique variants could lead to β grains with this orientation. The reconstruction of β grains of the small and the large-area images are performed with the same methodology. No major differences are observed in the reconstruction quality at different resolutions.

3.3. Volume fraction of variants

Characterization of the distribution of volume fraction of the 12 variants is integral to the construction of an effective crystal plasticity constitutive model, in which the material response corresponds to the volume fraction-weighted contribution from each of the 12 variants. For ensuring an unbiased sampling and reconstruction of the volume fraction distribution, the generation of statistically equivalent volume fractions for each of the variants must conform to the following five constraints.

(i) The distribution of variants with non-zero volume fractions within a parent β grain must be similar to the observed distribution over many samples, as shown in Fig. 4(a).
(ii) The total volume fraction of all variants at a material point must add up to $\sum_{i=1}^{12} v_f^i = 1$.
(iii) The distribution of volume fractions within a parent β grain must conform to the empirical distribution, as shown in Figs. 4(d, e, f).
(iv) The total volume fraction of each variant should reflect the global average of each variant, as shown in Fig. 4(b)
(v) Pairwise correlation between variant volume fractions must be maintained.

The proposed methodology, satisfying all of the above conditions, is conducted using the following steps.

1. The distribution in Fig. 4(a) is directly sampled to obtain N number of α laths containing a non-zero volume fraction within a parent β grain satisfying constraint (i).
2. $N-1$ points are randomly sampled in the range [0, 1], and sorted in ascending order. Volume fractions are assigned to the distances between the values of this sorted list in this range. This implies that the first volume fraction is the difference between 0 and the lowest sampled value, the second is the difference between the lowest sampled value and the second lowest sampled value, etc.
3. The above operation is performed for a set number of times, 100 in this example, to generate a representative distribution of variant volume fractions over many possible β grains. It serves as an initial guess for matching the experimental distribution.
4. This trial set of variant volume fractions is matched with the experimental distribution through an algorithm, with an established goodness of fit metric having a set baseline value. The Kolmogorov–Smirnov test statistic:

$$KS_{Ref} = \max_x(\|F_{Syn}(x) - F_{Exp}(x)\|),$$

defined as the maximum difference between cumulative distribution functions (CDFs) of the experimentally observed samples $F_{Exp}(x)$ and the initial synthetically generated samples $F_{Syn}(x)$ is selected for this purpose.
5. Next, one of the 100 β grains is randomly selected. One point in the set of $N-1$ points is randomly perturbed, while maintaining a minimum spacing of 0.01 between all other points in the [0, 1] range.

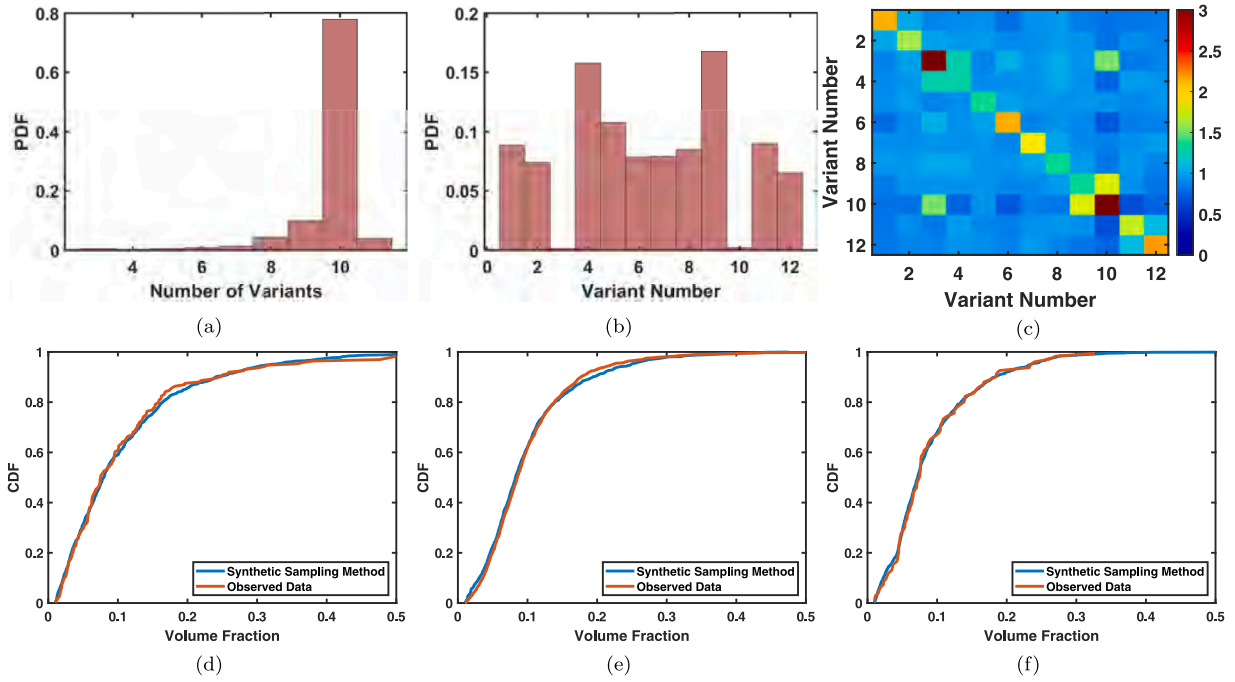

Fig. 4. (a) Histogram of probability density function (PDF) of the number of variants experimentally observed in a parent β grain, (b) PDF of volume fraction of variant ID numbers, (c) Correlation matrix c_{ij} of variant IDs relative to predicted values based on the total volume fraction; Comparing CDFs of variant volume fractions within a parent β grain with that generated by the synthetic sampling method for: (d) β grain $N = 9$, (e) β grain $N = 10$, and (f) β grain $N = 11$.

6. The CDF of this modified trial distribution is subsequently calculated and the Kolmogorov–Smirnov test statistic is computed and stored as KS_{Tr}. If this perturbation improves the test statistic, i.e. $KS_{Ref} > KS_{Tr}$, then this modification is retained, otherwise, it is discarded.
7. This iteration is continued until a convergence criterion is met, or a specified number of iterations are reached.

This approach satisfies constraints (ii) and (iii). The resulting distributions are compared for $N = 9$, 10, 11 in Figs. 4(d, e, f) respectively with satisfactory agreement.

The preference for variants in the microstructure is not necessarily uniform and depends on a multitude of material processing factors, including residual stresses, temperature gradients, cooling rates etc. (Shi and Wang, 2013), thus favoring particular variants. The volume fraction of individual variants v_f^i over the entire domain is shown in Fig. 4(b). Following the assignment of all of the volume fractions, the variant ID's to which the volume fractions are assigned are shuffled to satisfy the overall distributions of volume fractions shown in Fig. 4(b). This process satisfies constraint (iv). As shown in Shi and Wang (2013), there are particular interactions between variants that are energetically favored during the formation of the Widmanstätten microstructure. To determine if there are such pairings between the variants, a covariance-like metric is defined to determine the volume-weighted frequency of observed variant pairings, relative to their expectation expressed as:

$$c_{ij} = \frac{1}{N_\beta} \sum_{k=1}^{N_\beta} \frac{v_{f_k}^i v_{f_k}^j}{\bar{v}_f^i \bar{v}_f^j} \tag{6}$$

where $\bar{v}_f^j$ is the volume-averaged fraction of the jth variant, and $N_\beta = 12$. As shown in Fig. 4(c) the presence of any one variant does not influence the likelihood of the presence of another variant in an averaged sense. In other words, c_{ij} does not deviate from 1 on off-diagonal terms sufficiently to warrant the additional model complexity of including a covariance matching scheme, satisfying constraint (v). It should be noted that the high covariance of variants 3 and 10 is likely due to random noise on account of their minuscule sample size.

3.3.1. Statistics of α laths

Statistical characterization of the α laths in the 3D Widmanstätten microstructure is central to the crystal plasticity constitutive model discussed in Section 4, which incorporates α laths statistics. The constitutive model assumes that α lath boundaries form barriers to dislocation glide on slip planes, affecting the free motion of dislocations. This provides a basis for the determination of a mean-free path for dislocation glide on different slip systems in the α lath, to be incorporated in Hall–Petch type relations. The α lath morphology is approximated as a 3D ellipsoid. This geometric representation of the α lath is statistically representative with respect to morphological parameters, while maintaining a relatively low complexity and high parametrizability. In this analysis, a

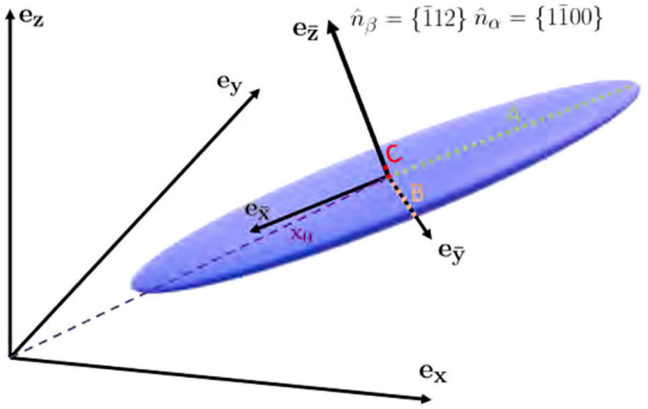

Fig. 5. Schematic showing the principal axes of the representative 3D ellipsoid, as well as the crystallographic relationship between the minor axis $\mathbf{e}_{\bar{z}}$ α lath and the $\{\bar{1}12\}$ crystallographic direction of the parent β grain.

single 3D ellipsoid is assigned to each variant within a parent β grain, effectively assuming a single 3D ellipsoid to approximate the morphology of all α laths of that variant within the β grain. A representative 3D ellipsoid shown in Fig. 5 is parametrically represented in the principal coordinate system, with its origin at the centroid, as:

$$\left(\frac{\bar{x}}{A}\right)^2 + \left(\frac{\bar{y}}{B}\right)^2 + \left(\frac{\bar{z}}{C}\right)^2 = 1 \tag{7}$$

where $A \geq B \geq C$ are semi-major, intermediate, and semi-minor axis lengths respectively. A position vector in the principal coordinate system is expressed as $\bar{\mathbf{x}} = \bar{x}\mathbf{e}_{\bar{x}} + \bar{y}\mathbf{e}_{\bar{y}} + \bar{z}\mathbf{e}_{\bar{z}}$, where $\mathbf{e}_{\bar{x}}, \mathbf{e}_{\bar{y}}, \mathbf{e}_{\bar{z}}$ are unit vectors along the major, intermediate and minor axes, and $\bar{x}, \bar{y}, \bar{z}$ are the respective components. The process of generating the ellipsoids starts with the identification and segmentation of 2D ellipses obtained in Section 3.1, along with the acquisition of the axis lengths, variant ID, and crystallographic orientation of the α and β laths. For each of these 2D ellipses, multiple trial 3D ellipsoids are generated, from which the most probable 3D ellipsoid from this set is determined and assigned homogeneously within a parent β grain.

As shown in Lütjering and Williams (2007), there is a relationship between the crystallographic direction $\mathbf{n}_\beta = \{\bar{1}12\}$ of the parent β grain and the minor axis $\mathbf{e}_{\bar{z}}$ of the 3D ellipsoid representing the α lath. According to this relation, the minor axis $\mathbf{e}_{\bar{z}}$ is written in the reference frame of the sample as:

$$\mathbf{e}_{\bar{z}} = \mathbf{G}^{-1}\mathbf{S}_i^\beta \frac{\mathbf{n}_\beta}{|\mathbf{n}_\beta|} \tag{8}$$

where $\mathbf{S}_i^\beta$ represents the symmetry for the ith variant described in Table 1, and $\mathbf{G}$ is defined as a rotation matrix that transforms a vector from the reference coordinates to the crystallographic coordinates of the parent β grain.

The *most probable* 3D α lath ellipsoid conforming to the crystallographic relation in Eq. (8), is determined from a sample size of fifty generated trial ellipsoids. Upon establishing the direction for $\mathbf{e}_{\bar{z}}$, the other two orthogonal principal axes with unit vectors $\mathbf{e}_{\bar{x}}$ and $\mathbf{e}_{\bar{y}}$ are selected randomly about the $\bar{z}$ axis. Subsequently, the most probable ellipsoid aspect ratios A/C and A/B are determined through a sampling process, in which the 2D ellipse formed by the intersection of the trial 3D ellipsoids with a centroidal XY plane, best matches the observed ellipse aspect ratios from EBSD scans. Finally, with known aspect ratios, the overall size of the ellipsoid is obtained through an estimation of the principal axis lengths (A, B, C). This process involves calculating the relationship between (A, B, C) of the 3D ellipsoid, and the semi-minor axis of the 2D ellipse formed by the intersection of the most probable 3D ellipsoid and the XY plane. The length of the semi-minor axis of the 2D ellipse is estimated by randomly selecting from the measured axis lengths of the 2D ellipse set corresponding to experimental EBSD maps. Checks are conducted to ensure that the semi-minor axis length C is not less than the minimum of the set of measured 2D ellipse axis length in EBSD scans.

Results of the 3D α lath ellipsoid generation process for the as-built and HIP-treated additively manufactured Ti-6Al-4V microstructure are shown in Figs. 6. The plots include distributions of the resulting aspect ratios A/C, A/B, B/C, and the size of the semi-major axis A. For all quantities, a log-normal distribution is used to parametrize the distributions with a good fit. The aspect ratio distributions for the as-built and HIP-treated samples are generally quite similar. However, the size of the α laths is much larger for the HIP-treated samples. This plays an important role in the overall mechanical response of the material.

3.4. Parent beta grain statistics and reconstruction

The morphological and orientation statistics of the parent β grains are extracted from the low-resolution orthogonal XY and XZ large-area images and processed using the DREAM.3D software (Groeber and Jackson, 2014). The overall microstructural morphology is well represented by elongated grains in the build direction. The SEMVEs are generated in the DREAM.3D framework. The aspect ratio of the β grain morphology in the build direction is characterized from the statistics of the XZ images, while the

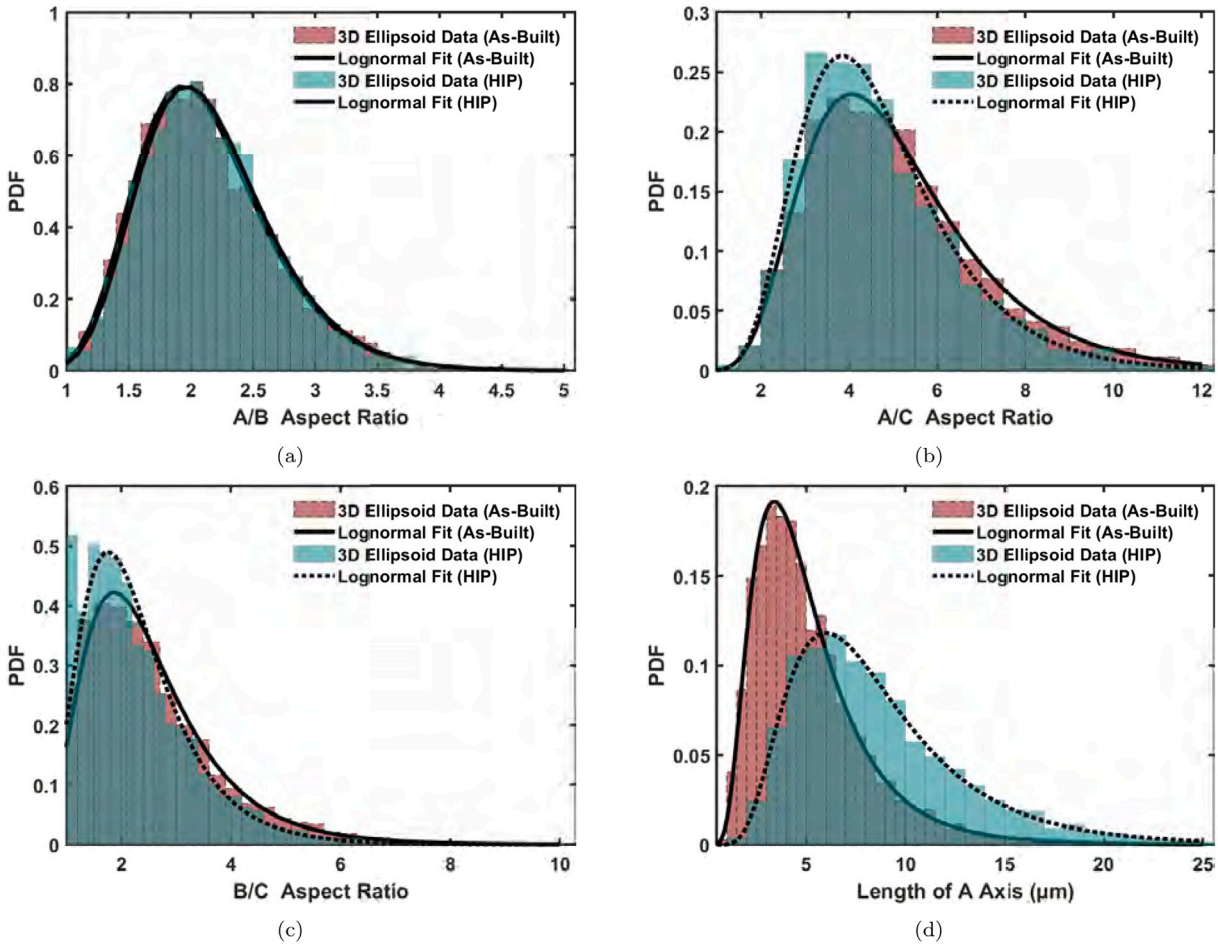

Fig. 6. Probability density functions of the aspect ratios and semi-major axis lengths of the most probable 3D ellipsoid: (a) A/B aspect ratio distribution, (b) A/C aspect ratio distribution, (c) B/C aspect ratio distribution, and (d) Size distribution of the semi-major axis A.

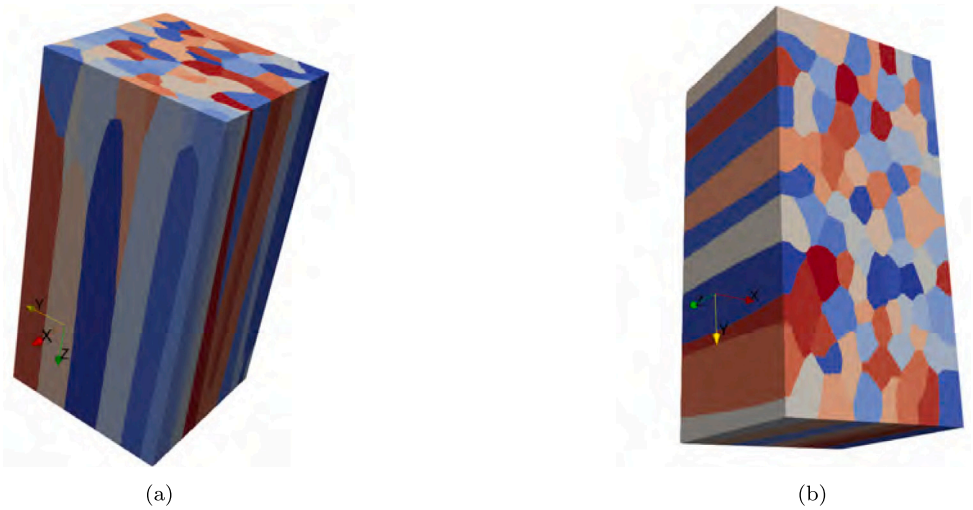

Fig. 7. Reconstructed SEMVEs of the parent β grain for two orthogonal directions corresponding to (a) vertical loads and (b) horizontal loads.

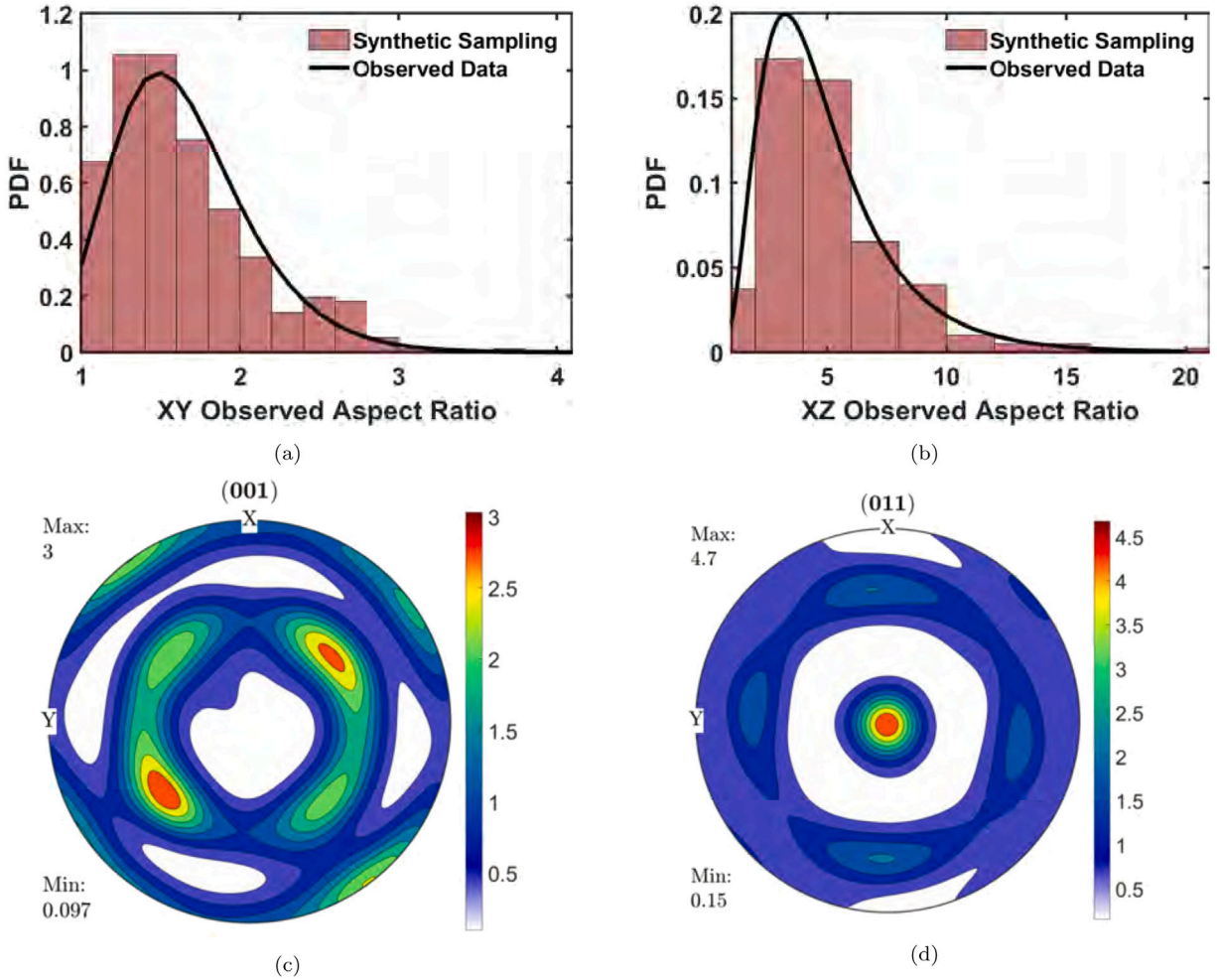

Fig. 8. Aspect ratio of the 3D ellipsoid representing β grains (a) A/B and (b) A/C; orientation distribution of the parent β grains showing (c) (001) pole figure and (d) (011) pole figure.

statistics from the XY images are used to describe the grain morphology perpendicular to the build direction. The overall A/B and A/C aspect ratios are plotted in Fig. 8(a, b). Two sets of 5 microstructural SEMVEs in the orthogonal directions (vertical and horizontal) are constructed as shown in Figs. 7 respectively, with each SEMVEs containing approximately 85 β grains. The overall SEMVE dimensions are 400 μm × 200 μm × 200 μm. The elongated grains are in the build direction and are textured to favor the (110) direction. The orientation distribution of the parent β grains showing (001) and (011) pole figures are shown in Figs. 8(c, d).

4. Crystal plasticity model accounting for α lath variants and porosity

The deformation behavior of the equivalent parent β grains with a statistical representation of the 12 α lath variants in the additively manufactured Ti-6Al-4V with Widmanstätten microstructure is modeled by an effective finite deformation, crystal plasticity model. The model accounts for all HCP slip systems pertaining to the α lath representation in the parent grains. Furthermore, the model incorporates porosity and its evolution with the material state, in consideration of the effect of void distribution in the microstructure. The effective crystal plasticity model for the equivalent parent β grains in the Widmanstätten microstructure is built on homogenization concepts introduced in Deka et al. (2006). The porosity evolution law follows developments in Yang and Ghosh (2022), which has developed an effective constitutive model for porous viscoplastic HCP crystals, capturing the effect of initial porosity, crystallographic orientation, void growth, stress triaxiality, and Lode parameters. Furthermore, it also accounts for a variety of loading cases, viz. compressive and tensile loading, low to high stress triaxialities, and uniaxial, biaxial and triaxial loading. This model is based on the variational framework in DeBotton and Castañeda (1995) and its phenomenological extensions in Han et al. (2013), Ling et al. (2016). Phenomenological extension parameters are introduced into the effective plastic potential to relax the assumptions employed in Han et al. (2013), Ling et al. (2016).

In the following, the equations refer to the evolution of state variables for any one of the 12 potential variants. The stress–strain relationship in the effective crystal plasticity model is written in the intermediate configuration in terms of the Mandel stress, given as (Yang and Ghosh, 2022):

$$\mathbf{M} = \mathbf{C}_e \hat{\mathbf{S}} \tag{9}$$

where $\mathbf{C}_e = \mathbf{F}_e^{\mathrm{T}} \mathbf{F}_e$ is the right Cauchy–Green tensor and $\mathbf{F}_e$ is the elastic part of the deformation gradient, defined as $\mathbf{F}_e = \mathbf{F}\mathbf{F}_p^{-1}$. Here $\mathbf{F}$ and $\mathbf{F}_p$ represent the total deformation gradient and the plastic deformation gradient, respectively. The second Piola–Kirchhoff stress tensor $\hat{\mathbf{S}}$ in the intermediate configuration is expressed as:

$$\hat{\mathbf{S}} = \mathbb{C}\mathbf{E}_e \tag{10}$$

where $\mathbb{C}$ represents a fourth-order anisotropic elasticity tensor, and $\mathbf{E}_e = \mathbf{C}_e - \mathbf{I}$ is the Green–Lagrange strain tensor. Plastic deformation for the porous crystalline material is not volume-preserving i.e. $det\mathbf{F}_p \neq 1$. The plastic velocity gradient tensor in the intermediate configuration for a porous HCP variant in the parent grain with void volume fraction f is given as (Yang and Ghosh, 2022; Han et al., 2013; Ling et al., 2016):

$$\mathbf{L}_p = \sum_{i}^{N_{SF}} (1 - w_1^i f) \sum_{\alpha}^{N_{slip}^i} \frac{\partial e_*^\alpha}{\partial \tau_*^\alpha} \frac{\partial \tau_*^\alpha}{\partial \mathbf{M}} \tag{11}$$

where for each variant, e_*^α is an effective slip potential function, w_1^i is a potential function parameter, and τ_*^α is the effective resolved shear stress. N_{SF} represents the total number of slip families, and N_{slip}^i is the number of slip systems in the ith slip family. For HCP crystals $N_{SF} = 5$ corresponding to the $\langle a \rangle$-basal, $\langle a \rangle$-prismatic, $\langle a \rangle$-pyramidal, $\langle c + a \rangle$ pyramidal I, and $\langle c + a \rangle$ pyramidal II slip families. The effective slip potential e_α^* is expressed as:

$$e_\alpha^* = \frac{\dot{\gamma}_0^\alpha}{m+1} \left(\frac{\tau_*^\alpha}{\bar{g}_0^\alpha} \right)^{m+1} \tag{12}$$

where $\bar{g}_0^\alpha$ is the initial slip-system resistance given in Eq. (17), and $\dot{\gamma}_0^\alpha$ and m are the reference slip-rate and rate sensitivity exponent respectively. The porosity or void volume fraction f evolves according to the relation:

$$\dot{f} = (1 - f)\mathrm{Tr}(\mathbf{L}_p) \tag{13}$$

where Tr corresponds to the trace of a matrix. The effective resolved shear stress on the α slip system τ_α^*, is iteratively solved by satisfying the following equation:

$$\left(\frac{\tau^\alpha}{\tau_*^\alpha} \right)^2 + w_3^\alpha w_1^\alpha f \frac{M_{eq}^2}{(\tau_*^\alpha)^2} + 2 f w_1^\alpha \cosh\left(w_2{}^\alpha \frac{M_m^2}{\tau_*^\alpha} \right) - 1 - (w_1^\alpha f)^2 = 0 \tag{14}$$

where $M_m = -\frac{1}{3} Tr(\mathbf{M})$ is the hydrostatic part of the Mandel stress and $M_{eq} = \sqrt{\frac{3}{2} M_{ij} M_{ij}}$ represents the equivalent Mandel stress. The resolved shear stress on the α slip plane is expressed as $\tau_\alpha = \mathbf{M} : \mathbf{s}_0^\alpha$ where the Schmid tensor is defined as $\mathbf{s}_0^\alpha = \mathbf{m}_0 \otimes \mathbf{n}_0$ for a slip normal $\mathbf{n}_0$ and slip direction $\mathbf{m}_0$. The potential function parameters $w_1^\alpha, w_2^\alpha, w_4^\alpha$ are given by the set of equations (Yang and Ghosh, 2022):

$$\begin{aligned} w_1^\alpha &= a_1^\alpha + b_1^\alpha \tanh\left(-d_1^\alpha \left(\frac{f - f_0}{f_0} \right) \right) \\ w_2^\alpha &= a_2^\alpha + b_2^\alpha \tanh\left(-d_2^\alpha \left(\frac{f - f_0}{f_0} \right) \right) \\ w_4^\alpha &= 1 + \tanh\left(-d_4^\alpha \left(\frac{f - f_0}{f_0} \right) \right) \end{aligned} \tag{15}$$

Values of the constant coefficients a_1^α, b_1^α, d_1^α, a_2^α, b_2^α, d_2^α, d_4^α, and w_3^α for different slip systems have been calibrated in Yang and Ghosh (2022) and are given in Appendix B. The plastic slip rate $\dot{\gamma}^\alpha$ for a given slip system is given by a power-law form of the flow rule as:

$$\dot{\gamma^\alpha} = \dot{\bar{\gamma}}^\alpha \left\langle \frac{|\tau_*^\alpha - \chi^\alpha| - \tau_{GP}^\alpha}{g^\alpha + \tau_{GF}^\alpha} \right\rangle^{\frac{1}{m}} \mathrm{sign}\left(\tau_*^\alpha - \chi^\alpha \right) \tag{16}$$

where $\langle\rangle$ is the Macaulay bracket, $\dot{\bar{\gamma}}^\alpha$ is the reference slip rate, m is the rate-sensitivity exponent, and χ^α is the back-stress on a particular slip system. The resolved shear stress components τ_{GP}^α and τ_{GF}^α contribute to the parallel and forest geometrically necessary dislocations (GNDs) respectively. The temperature-dependent slip-system resistance due to statistically stored dislocations for the α slip system is expressed as (Ozturk et al., 2016):

$$g^\alpha(\theta) = \bar{g}_0^\alpha + g_{HP}^\alpha - \hat{g}^\alpha \left(1 - \exp\left(\frac{\theta - \theta_{ref}^\alpha}{\hat{\theta}^\alpha} \right) \right) \tag{17}$$

where $\bar{g}_0^\alpha$ is the initial slip-system resistance, g_{HP}^α corresponds to the contribution from grain size effect and $\hat{g}^\alpha$ is a scaling parameter for its temperature dependence. The temperature-dependent constants $\bar{g}_0^\alpha$, $\hat{g}^\alpha$, θ_{ref}^α and $\hat{\theta}^\alpha$ have been calibrated in Ozturk et al. (2016) and are given in Appendix B. The size dependent contribution is attributed to the Hall–Petch effect as:

$$g_{HP}^\alpha = \frac{K}{\sqrt{D^\alpha}} \tag{18}$$

where K is the Hall–Petch coefficient, calibrated in Venkataramani et al. (2008) is given in Appendix B. D^α is the mean free-path or traversable length of a dislocation in the slip direction m_0^α across the α lath, whose morphology is characterized by Eq. (7) for a 3D ellipsoid shown in Fig. 5. The distance traversed by a dislocation in the m_0^α direction through the center of the ellipsoid is given by

$$D^\alpha = \sqrt{[A(\mathbf{e}_{\tilde{\mathbf{x}}\cdot m_0^\alpha})]^2 + [B(\mathbf{e}_{\tilde{\mathbf{y}}\cdot m_0^\alpha})]^2 + [C(\mathbf{e}_{\tilde{\mathbf{z}}\cdot m_0^\alpha})]^2} \tag{19}$$

The evolution of the hardening rate is given as:

$$\dot{g}^\alpha(t) = \sum_{\beta=1}^{N_{slip}} \tilde{q}^{\alpha\beta} h^\beta \left|\dot{\gamma}^\beta\right| \tag{20}$$

where $\tilde{q}^{\alpha\beta}$ represents the latent hardening matrix and the self-hardening contribution h^β is given by Venkatramani et al. (2006):

$$h^\beta = h_0^{\beta*}\left|1 - \frac{g^\beta}{g_s^\beta}\right|^r \operatorname{sign}\left(1 - \frac{g^\beta}{g_s^\beta}\right) \quad , \quad g_s^\beta = \tilde{g}_s{}^\beta \left(\frac{\dot{\gamma}^\beta}{\hat{\dot{\gamma}}}\right)^n \tag{21}$$

Here n, r, and $\tilde{g}_s^\beta$ are hardening parameters described in Deka et al. (2006), g^β is the slip-system saturation deformation resistance and h^β is the slip hardening rate, given as:

$$h_0^{\beta*} = h_0^\beta w_4^\alpha \tag{22}$$

h_0^β is the initial slip hardening rate that has calibrated in Yang and Ghosh (2022) and given in Appendix B.

An Armstrong–Frederick type law (Frederick and Armstrong, 2007) is used for back-stress evolution, expressed as:

$$\dot{\chi}^\alpha = c\dot{\gamma}^\alpha - d\,\chi^\alpha\left|\dot{\gamma}^\alpha\right| \tag{23}$$

where c and d are parameters calibrated in Ozturk et al. (2016). Hardening is attributed to GNDs for parallel and forest interactions and is described by the following equations:

$$\tau_{GP}^\alpha = c_1^\alpha G^\alpha b^\alpha \sqrt{\rho_{GP}^\alpha + \rho_{AP}^\alpha}, \quad \tau_{GF}^\alpha = \frac{Q^\alpha}{c_2^\alpha b^{\alpha 2}} \sqrt{\rho_{GF}^\alpha + \rho_{AF}^\alpha} \tag{24}$$

where ρ_{GP}^α and ρ_{GF}^α respectively represent GND densities parallel and normal to the slip plane α. They are calculated from the Nye tensor $\boldsymbol{\Lambda} = \nabla \times \mathbf{F}_p$ as detailed in Ozturk et al. (2016). The coefficients can be found in Appendix B. ρ_{AP}^α and ρ_{AF}^α terms are GND augmentation terms described next.

4.1. Augmented GND density accounting for lath boundaries

The calculation of GND density from the Nye tensor $\boldsymbol{\Lambda} = \nabla \times \mathbf{F}_p$ requires the explicit crystallographic representation of individual grains and their boundaries in the microstructure. Due to the lack of this explicit α lath boundary representation in the equivalent crystal model, the $\nabla \times \mathbf{F}_p$ term due to dislocation pileup is significantly smaller than in models with explicitly represented crystal boundaries. It is necessary to augment the effective crystal plasticity model, which does not explicitly incorporate α lath boundaries within the parent β grains, to compensate for the lower GND densities affecting plastic hardening. The enhancement is taken from a model in Ashby (1970), where GND densities are approximated for a matrix with plates that are assumed to be impenetrable to dislocations, separated by a distance D^α. The augmented GND density is given as:

$$\rho_{GND}^\alpha = c_5 \frac{\gamma^\alpha}{b^\alpha D^\alpha} \tag{25}$$

where γ^α represents the cumulative slip on a slip system α, and b represents the length of the Burgers vector. The parallel and forest augmented GND densities are related to the total augmented GND density by the relations:

$$\rho_{AF}^\alpha = \sum_\beta^N \chi_{AF}^{\alpha\beta} |\rho_{GND}^\beta \sin(n^\alpha, t^\beta)| \, , \quad \rho_{AP}^\alpha = \sum_\beta^N \chi_{AP}^{\alpha\beta} |\rho_{GND}^\beta \cos(n^\alpha, t^\beta)| \tag{26}$$

As discussed in Ozturk et al. (2016), $\chi_{AF}^{\alpha\beta}$ represents the interaction matrix between slip systems. For a specified deformation gradient $\mathbf{F}$ applied to a β grain, the above set of equations evolves separately for each of the 12 variants. Since this augmentation is not dependent on the term $\nabla \times \mathbf{F}_p$ for the Nye tensor, this approach is not dependent on the mesh resolution.

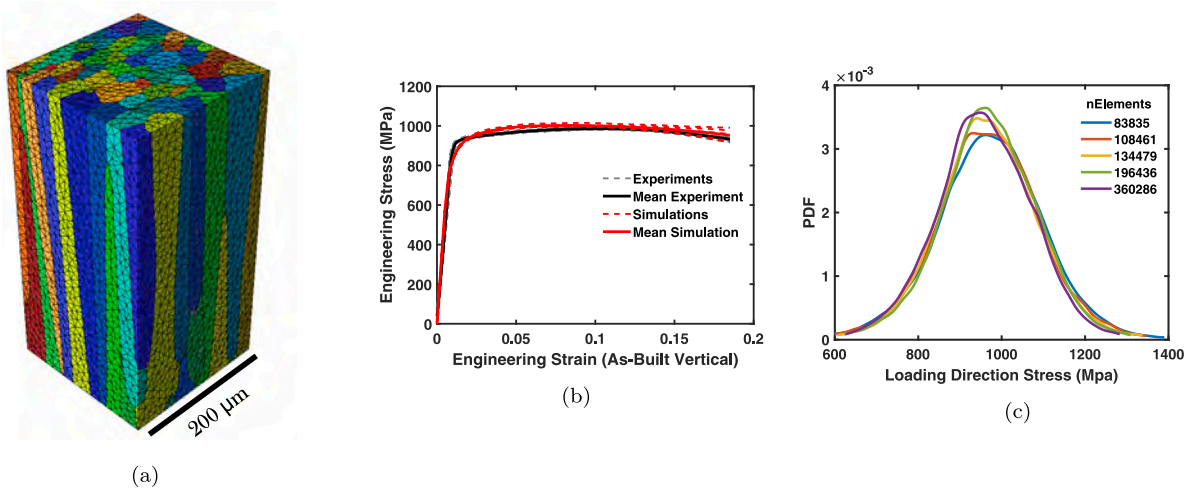

Fig. 9. (a) A single instantiation of the SEMVE of the parent β grains (shown with different colors) containing approximately 85 grains, (b) comparison of the engineering stress–strain response of 5 SEMVE instantiations, and their mean, with experimental data acquired in Section 2.3, and (c) comparison of the probability density function of loading direction Cauchy stress for 5 different mesh resolutions. (For interpretation of the references to color in this figure legend, the reader is referred to the web version of this article.)

4.2. Stresses at a material point

The above equations correspond to the evolution of state variables in a single α lath variant, for a given deformation gradient $\mathbf{F}$. Evaluating the stresses at an element integration point in the FE model requires a volume fraction based weighting over all of the 12 variants. The Cauchy stress for the kth variant is given as:

$$\boldsymbol{\sigma}^{(k)} = \frac{1}{\det \mathbf{F}_e^{(k)}} \mathbf{F}_e^{(k)-\mathrm{T}} \mathbf{M}^{(k)} \mathbf{F}_e^{(k)\mathrm{T}} \tag{27}$$

The corresponding stress tensor for a material point is expressed as the sum over all the 12 variants as:

$$\boldsymbol{\sigma} = \sum_{k=1}^{12} v_f^{(k)} \boldsymbol{\sigma}^{(k)} \tag{28}$$

The state variables of each variant evolve independently, and are not related to one another. This method is substantially more efficient than if all of the α laths were explicitly represented and simulated.

4.3. Calibration of the crystal plasticity model

The crystal plasticity and porosity evolution parameters, given in Tables 5–8, are adopted from prior work in Ozturk et al. (2016), Yang and Ghosh (2022), Venkataramani et al. (2008). In these papers, the crystal plasticity parameters are calibrated using experimental results for a wide range of strain-rates and loading conditions. For calibrating additional parameters related to the additively manufactured Ti-6Al material, the first of the material-load direction sets in Section 2.3, is simulated. For this process, 5 SEMVEs are generated for the set by following the steps in Section 3 with randomly-generated, different initial conditions. Voxelized representations of the generated SEMVEs are meshed with 4-noded tetrahedral (TET4) elements, using the meshing package Simmetrix (Simmetrix Inc., 2015). The resultant microstructures contain approximately 175k elements and an example instantiation with mesh is shown in Fig. 9(a). The average volume of the α laths in the SEMVE are 96 μm^3 for the as-built material microstructure, and 468 μm^3 for the HIP-treated material microstructure. This corresponds to approximately 168,000 and 35,000 α laths for the SEMVEs of the as-built and HIP-treated materials respectively. Displacement boundary conditions are applied on the model corresponding to a strain rate of 10^{-3} up to a final engineering strain of 18.5%. Minimum boundary conditions (MBCs), preventing rigid body motion, are applied on the SEMVE boundary. Given that the size difference between the SEMVE and the experimental specimen is not very large (~10), the MBCs are deemed appropriate as they allow instabilities like necking to occur in the SEMVE, as seen in the actual specimen. Applying periodic boundary conditions on the SEMVE can over-constrain the deformation modes and may inhibit these instabilities. The calibration process evaluates parameters to match the experimental stress–strain response as shown in Fig. 9(b). The corresponding optimized parameters are given in Table 3.

For the calibration process, a metric corresponding to the percentage error in the loading direction stress component σ is minimized. For two arbitrary stress–strain curves $\sigma_a(\epsilon)$ and $\sigma_b(\epsilon)$ the metric is given as:

$$\Phi(\sigma_a(\epsilon), \sigma_b(\epsilon)) = \frac{1}{max(\sigma_a)\epsilon_{final}} \int_0^{\epsilon_{final}} |\sigma_a(\epsilon) - \sigma_b(\epsilon)| d\epsilon \tag{29}$$

Table 3
Calibrated additional crystal plasticity model parameters.

Description	Symbol	Value(s)
Augmented GND Coefficient	c_5	3
Initial Basal Slip resistance	$\tilde{g}_0^{Basal}$	206 (MPa)
Initial Prismatic Slip resistance	$\tilde{g}_0^{Prismatic}$	203 (MPa)
Initial Pyramidal $\langle a \rangle$ Slip resistance	$\tilde{g}_0^{Pyramidal\langle a \rangle}$	309 (MPa)
Initial Pyramidal $< a+c >$ I Slip resistance	$\tilde{g}_0^{Pyramidal<a+c>I}$	400 (MPa)
Initial Pyramidal $< a+c >$ II Slip resistance	$\tilde{g}_0^{Pyramidal<a+c>II}$	400 (MPa)

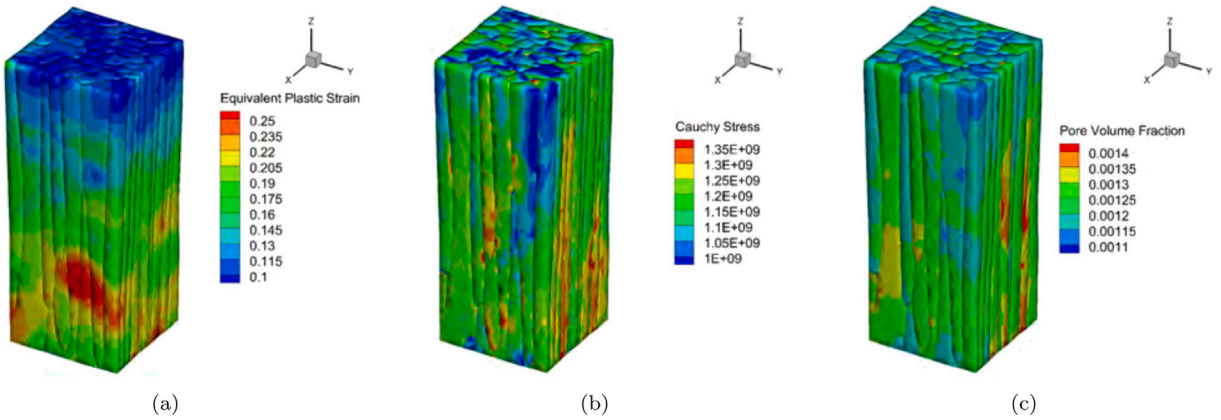

Fig. 10. Contour plots of (a) equivalent plastic strain, (b) Cauchy stress, and (c) void volume fraction in a SEMVE of the parent β grain at 18.5% strain.

The error metric for the experimental and simulation data is measured by $\Phi(\bar{\sigma}_{exp}(\epsilon), \bar{\sigma}_{sim}(\epsilon))$, where $\bar{\sigma}_{exp}(\epsilon) = \frac{1}{N_{exp}} \sum_{i=1}^{N_{exp}} \sigma^i_{exp}(\epsilon)$ and $\bar{\sigma}_{sim}(\epsilon) = \frac{1}{N_{sim}} \sum_{i=1}^{N_{sim}} \sigma^i_{sim}(\epsilon)$ are respectively the mean engineering stress–strain responses for all experiments and simulations in the set. A value $\Phi(\bar{\sigma}_{exp}(\epsilon), \bar{\sigma}_{sim}(\epsilon)) = 0.019$ corresponds to a $\sim 1.9\%$ difference in the average stress for strains ranging from 0 to 18.5%. Similar metrics for purely experimental and simulation data correspond to the average level of deviation in the data,

$$\bar{\Phi}_{exp} = \frac{1}{N_{exp}} \sum_{i=1}^{N_{exp}} \Phi(\bar{\sigma}_{exp}(\epsilon), \sigma_{exp}(\epsilon)^i) \quad \text{and} \quad \bar{\Phi}_{sim} = \frac{1}{N_{sim}} \sum_{i=1}^{N_{exp}} \Phi(\bar{\sigma}_{sim}(\epsilon), \sigma_{sim}(\epsilon)^i) \tag{30}$$

The metrics are computed to be $\bar{\Phi}_{exp} = 0.0067$ and $\bar{\Phi}_{sim}(\epsilon) = 0.0082$.

The contour plots of the simulated equivalent plastic strain, Cauchy stress, and porosity in the SEMVE at the final strain of 18.5% strain are depicted in Fig. 10. The equivalent plastic strain contour plot in Fig. 10(a) shows substantial variation, including plastic localization with the onset of necking. The evolving void volume fraction and the Cauchy stress in Figs. 10(b, c) also show significant variations. This stochastic material response is attributed to a combination of the spatial variations in α lath statistics and the parent β grain morphology.

The porosity evolution is further compared to that for a single uniaxial strain test conducted under similar conditions in Benzing et al. (2020). The porosity or void volume fraction in this test was observed to have increased by 9%. The corresponding increase in the simulated void volume fraction f across the SEMVE instantiations is 15%, with f increasing from 0.11% to 0.127%, which is deemed to be satisfactory agreement.

A mesh sensitivity study is performed by meshing the vertically oriented microstructure in Fig. 9(a) with 5 different mesh densities, with the number of elements ranging from 84×10^3 to 360×10^3. The microstructure is loaded to a maximum of 2.5% engineering strain. The volume-averaged, loading direction stresses are found to be within 1% of each other for all the 5 meshes. Furthermore, the probability density functions (PDFs) of the loading direction stresses in the simulated microstructures are compared in Fig. 9(c). It is seen that the PDFs begin to converge at around 130 k elements. This convergence is further substantiated by the comparatively low values of the Kolmogorov–Smirnov test statistics (Dodge, 2008) between the distributions. The KS-test statistic between 360 k and 130 k elements is determined to be 0.0295. In contrast, the KS-test statistic between 360k and 84k elements is determined to be 0.0636. This test demonstrating a substantial decrease in error, and a sufficiency of 13 k elements, which is lower than the average 175 k elements used in the microstructural simulations. The computation time required for each of the mesh sensitivity test simulations scaled approximately linearly with the number of elements, to around 1.25 CPU-hours per 1000 elements for 48 Intel Xeon Gold 6248R parallel CPUs. For SEMVE simulations up to 18.5% engineering strain, approximately 6.12 CPU-hours are required per 1000 elements.

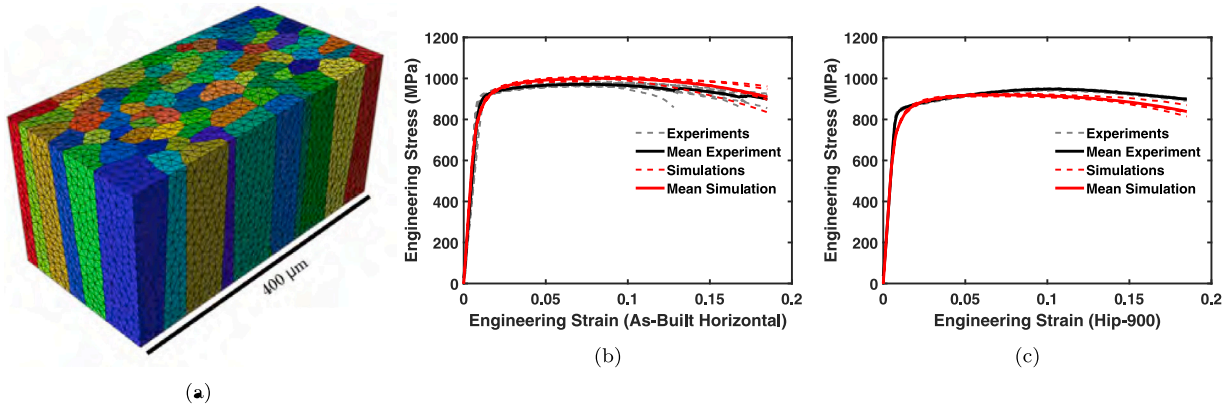

(a) (b) (c)

Fig. 11. (a) Mesh of a single instantiation of a SEMVE containing approximately 85 grains, where different colors represent different parent β grains. (b) The engineering stress, engineering strain relationship between the 5 as-built SEMVE instantiations loaded perpendicular to the build direction, and experimentally collected data. (c) The engineering stress, engineering strain relationship between the 5 HIP treated SEMVE instantiations loaded parallel to the build direction, and experimentally collected data. (For interpretation of the references to color in this figure legend, the reader is referred to the web version of this article.)

Table 4
The mean and standard deviation-based metrics, $\bar{\boldsymbol{\Phi}}_{exp}$, $\hat{\boldsymbol{\Phi}}_{exp}$, $\bar{\boldsymbol{\Phi}}_{sim}$, $\hat{\boldsymbol{\Phi}}_{exp}$, and $\boldsymbol{\Phi}(\bar{\sigma}_{exp}(\epsilon), \bar{\sigma}_{sim}(\epsilon))$ are respectively calculated from experimental, simulation, and experimental-simulation data for the three material-direction sets in the calibration and validation examples.

	Set 1 (C)		Set 2 (V)		Set 3 (V)	
	Mean ($\bar{\boldsymbol{\Phi}}$)	SD ($\hat{\boldsymbol{\Phi}}$)	Mean ($\bar{\boldsymbol{\Phi}}$)	SD ($\hat{\boldsymbol{\Phi}}$)	Mean ($\bar{\boldsymbol{\Phi}}$)	SD ($\hat{\boldsymbol{\Phi}}$)
Experimental data	0.0067	0.0020	0.0128	0.0037	0.0040	0.0027
Simulation data	0.0082	0.0044	0.0106	0.0080	0.0055	0.0044
Experiment-simulation	0.0190	N/A	0.0279	N/A	0.0714	N/A

5. Validation studies for the porous crystal plasticity model of the equivalent crystal

Validation is conducted with the second and third of the material-load direction sets in Section 2.3. As with the calibration, 5 SEMVEs are generated with different initial conditions, and simulated for identical loading conditions. An example model and mesh for the second set as-built material without heat treatment, loaded perpendicular to the build direction, is shown in Fig. 11(a). The simulated mechanical responses are compared with those from experiments in Fig. 11(b) with reasonably good agreement. The third set of HIP-treated material with minimal porosity that is loaded vertically, shares an almost identical parent β grain microstructure as the first set used in the calibration. Correspondingly, the model uses the same parent β grains and their meshes from the calibration example. However, the α statistics assigned to each β grain are significantly different. The mechanical response of the third material-direction set is shown in Fig. 11(c).

The $\boldsymbol{\Phi}$ metric in Eq. (29) is again used to quantify the error in stress–strain responses for the validation examples. The metric for all the 3 sets (as-built, as-built perpendicular and HIP-treated) are given in Table 4. For a more complete picture of the variation of individual instantiations, the standard deviations are also included in the table. The standard deviation of the $\boldsymbol{\Phi}$ metric for the experimental and simulation data are given as:

$$\hat{\boldsymbol{\Phi}}_{exp} = \sqrt{\frac{1}{N_{exp}-1}\sum_{i=1}^{N_{exp}}\left(\bar{\boldsymbol{\Phi}}_{exp} - \boldsymbol{\Phi}(\bar{\sigma}_{exp}(\epsilon), \sigma^{i}_{exp}(\epsilon))\right)^2}$$

$$\hat{\boldsymbol{\Phi}}_{sim} = \sqrt{\frac{1}{N_{sim}-1}\sum_{i=1}^{N_{sim}}\left(\bar{\boldsymbol{\Phi}}_{sim} - \boldsymbol{\Phi}(\bar{\sigma}_{sim}(\epsilon), \sigma^{i}_{sim}(\epsilon))\right)^2}$$

The results generally show good agreement between the experiments and simulations for the validation tests. The largest error is seen for the HIP-treated samples, possibly because of small discrepancies in the Hall–Petch effect coefficient in Eq. (18) accounting α lath size effects, as well as the localized plastic straining with necking in the HIP-treated microstructure as seen in Fig. 12.

6. Investigation on microstructural stochasticity

FE simulations are conducted for 5 SEMVE instantiations of each of the three material-direction sets, discussed in Section 2.3. These SEMVEs are generated with the statistical distributions of the variant volume fraction, α lath size and shape, and β grain size and shape conforming to the experimental EBSD maps. However, the stochasticity in various microstructural parameters

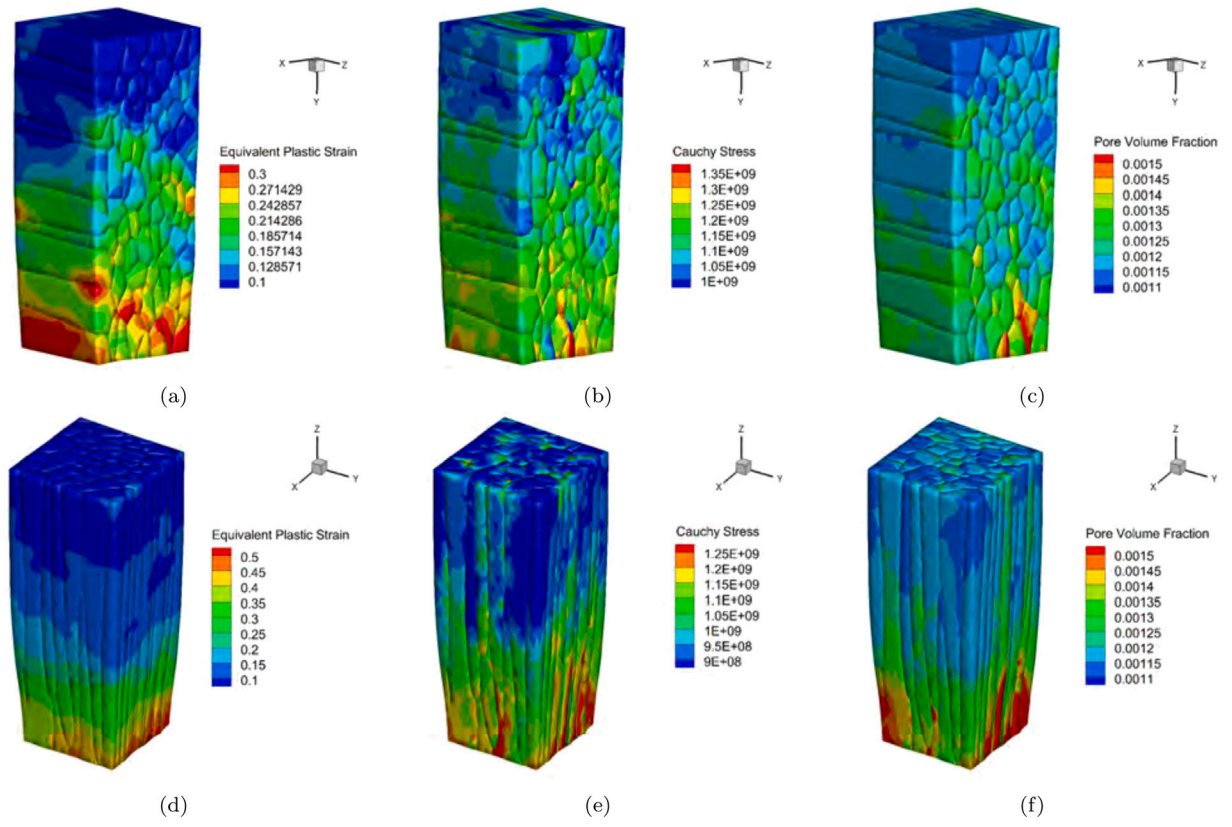

Fig. 12. Contour plots of (a) equivalent plastic strain, (b) Cauchy stress, and (c) porosity distribution in a SEMVE of the as-built material loaded perpendicular to the build direction (set 2) at 18.5% strain; Contour plots of (d) equivalent plastic strain, (e) Cauchy stress, and (f) porosity distribution in a SEMVE of the HIP-treated material loaded parallel to the build direction (set 3) at 18.5% strain.

in the SEMVEs that are not explicitly accounted for, result in significant variability in the simulated deformation-related state variables. Understanding the drivers of these variations through the effect of microstructural parameters and deformation variables on the overall material response, can provide useful insights on the deformation behavior of additively manufactured Ti-6Al-4V microstructures. State variables, viz. the Cauchy stress σ_{ij} in the loading direction, the equivalent plastic strain $\bar{\epsilon}^p$, and the local void volume fraction f, are studied in this section.

6.1. Variation attributable to the statistical moments of state variables

For assessing the effect of statistical moments of the state variables, the difference in loading direction engineering stresses at 18.5% engineering strain ${}^i\Delta^{ES}$ is plotted as a function of the mean and standard deviation of the stress, plastic strain, and void volume fraction in Fig. 13. For a given instantiation i, the difference in stresses is defined as:

$$ {}^i\Delta^{ES} = \sigma^i - \bar{\sigma}, \quad \text{where} \quad \bar{\sigma} = \frac{1}{N_{sim}} \sum_{i=1}^{N_{sim}} \sigma^i \tag{31} $$

$N_{sim} = 5$ for these plots. The mean and standard deviation are representative of the statistical moments of distributions of the state variables. Simple linear regression curves are generated for the data points in each plot and the corresponding coefficient of determination R^2 values are determined. The R^2 value corresponds to the proportion of the variation in stress difference with respect to the moments of the state variables. The higher R^2 values in the plots of figures Fig. 13(d, e, f) reveal that the variance of the distributions is much more predictive of the stress patterns. In addition to R^2, 95% confidence bounds are given for Pearson correlation coefficients.

6.2. Variation related to β microstructure and orientation

The parent β microstructures are strongly textured with elongated grains in the build direction. Determining the effect of individual microstructural instantiations is important to understanding the drivers of micromechanical variability and overall

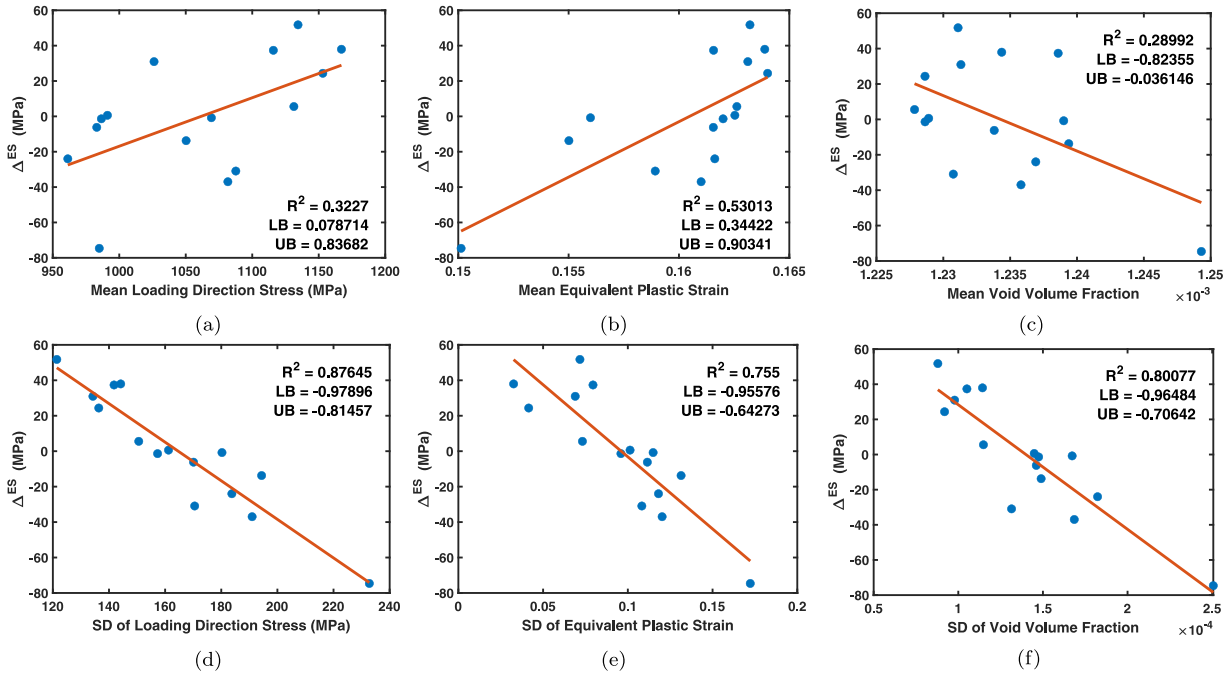

Fig. 13. The stress difference plotted as a function of the mean and standard deviation respectively of the (a, d) loading direction stress, (b, e) equivalent plastic strain, (c, f) void volume fraction, at 18.5% engineering strain. The figures include 95% confidence intervals for the Pearson correlation coefficients, marked by LB and UB respectively.

material properties. Since the vertical As-Built (AB) and HIP-treated (HT) microstructures have the same β grain structure and β orientations, the effect of the β microstructure instantiations can be understood by determining if state variables with the same β microstructure statistics but different α lath statistics are correlated. The effect of the β microstructure and orientations on the stress at 18.5% strain is determined by plotting the stress difference ${}^{i}\Delta_{HT}^{ES}$ vs. ${}^{i}\Delta_{AB}^{ES}$ from Eq. (31), at 18.5% strain in Fig. 14(a). A sustained correlation across samples indicates that instantiations of parent β grains have a significant effect on microstructural state variables. Furthermore, the plots of the standard deviation of the loading direction stress and effective plastic strain in Fig. 14(b, c) show their correlation. As there are little to no correlations between the instantiations, it is likely that instantiations of the β microstructure play a very small role in the variation of state variables.

7. Summary and conclusions

Building from a foundation of microstructural characterization, mechanical testing, 3D synthetic microstructures, and statistically equivalent microstructural volume elements (SEMVEs), and image-based microstructural modeling, this paper develops an effective crystal plasticity model with porosity evolution for additively manufactured Ti-6Al-4V alloys. The microstructure of these materials is characterized by a complex Widmanstätten morphology containing 12 α lath variants. The direct numerical simulation of microstructures with explicit representation of the α lath morphology is computationally prohibitive. To overcome this major bottleneck, it is necessary to create an effective crystal plasticity framework with a parametric representation of the α lath morphology. This is achieved by identifying the crystallographic relationship of the α laths in relation to the parent β grains from which they have nucleated, and developing methods to incorporate a statistical representation of HCP α laths in β grains. The constitutive model for β grains statistically account for the size, shape, orientation, and crystallography of all 12 α lath variants. An important contribution is the integration of porosity evolution with the crystal plasticity model.

Statistical characterization of α laths assumes a 3D ellipsoidal representation of the morphology. This process first generates equivalent 2D ellipses from orthogonal EBSD scans of the material microstructure Subsequently, the most probable 3D ellipsoids are obtained through the use of stereological concepts that equate the 2D intersection of ellipsoids with 2D EBSD-based maps. Statistical functions that characterize the distribution of observed 3D ellipsoids, and allow for their efficient and accurate statistical sampling are constructed thereafter. Subsequently, a prior β reconstruction algorithm is executed, allowing for the identification of the crystallographic orientation of the parent β grains. The morphology of the β grains are characterized, and used to generate statistically equivalent instantiations of the β grain microstructure using the DREAM.3D code. For each β microstructure, the distributions characterizing the α lath morphology are sampled. The combined statistics establish a statistically equivalent representative volume element or SEMVE that incorporates the physically relevant portions of the α laths in an explicit voxelized description of the much larger β microstructure.

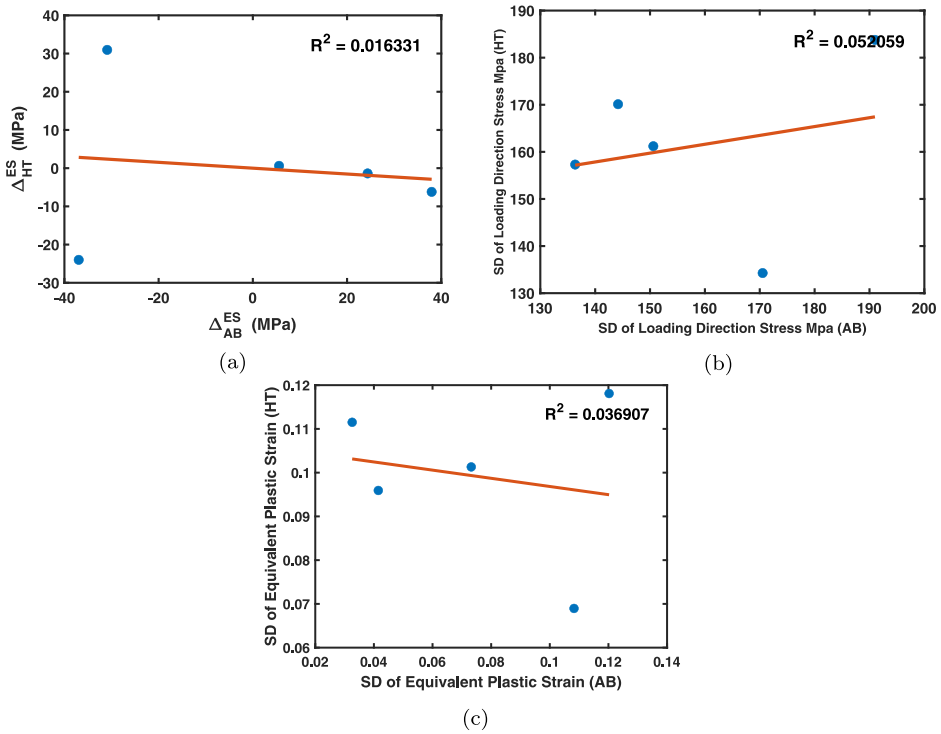

Fig. 14. (a) Plot of the difference in mean stress for the as-built (AB) microstructure loaded parallel to the build direction and the HIP-treated (HT) microstructure; Plot of the standard deviation of: (b) the Cauchy stress distribution for the (AB) and (HT) microstructures, (c) the equivalent plastic strain distribution for the (AB) and (HT) microstructures.

The calibration and validation of the effective crystal plasticity model incorporate results from three different sets of material-loading tests, viz. (i) as-built material loaded in the build direction, (ii) as-built case loaded perpendicular to the build direction, and (iii) a HIP-treated case loaded in the build direction. Set (i) is used for calibration, while the other two are used in validation. The validation tests demonstrate reasonably good accuracy of the model for tests corresponding to sets (ii) and (iii). The lower yield stress predicted for the HIP-treated materials due to the larger α laths is in good agreement with experimental observations. An insightful result of the model-based simulations infers that the standard deviation of the state variables are more predictive of the overall response than the mean.

The material model developed in this study, when integrated with process models, is expected to provide insights on optimizing the performance and qualification of additive manufacturing processes. By linking this approach with models that can accurately predict α lath morphology, β grain structure, and initial porosity from material processing conditions, superior material response predictions can be obtained.

CRediT authorship contribution statement

M. Pinz: Methodology, Software, Formal analysis, Writing – original draft. **J.T. Benzing:** Resources, Investigation. **A. Pilchak:** Methodology, Visualization. **S. Ghosh:** Conceptualization, Methodology, Supervision, Writing – review & editing, Funding acquisition.

Declaration of competing interest

The authors declare that they have no known competing financial interests or personal relationships that could have appeared to influence the work reported in this paper.

Acknowledgments

This work has been supported through Grant No. CMMI-1825115 from the National Science Foundation, United States of America awarded by the Mechanics of Materials and Structures (MOMS) Program (Program Manager: Dr. Siddiq Qidwai). Computational support for this work provided by the Rockfish clusters at Maryland Advanced Research Computing Center (MARCC) and Extreme Science and Engineering Discovery Environment (XSEDE) bridges-2 cluster at the Pittsburgh Supercomputing Center (PSC) is also gratefully acknowledged.

Appendix A. Pseudo code for determining β parent grain from α laths

Require: a set A of all segmented α_i grains with unassigned parent β grain, and orientation $\boldsymbol{\beta}_i$
Require: a set B of all segmented α_i grains that contain an assigned $\boldsymbol{\beta}_i$ orientation
while A is not empty **do**
for Select the next alpha grain (α_i) in A **do**
Initialize a set of α laths potentially sharing the same β grain $C = \emptyset$
for all neighbors j **do**
compute $\Delta\bar{\mathbf{q}}_{k*}^{ij}$
if $\min_l(|\Delta(\bar{\mathbf{q}}_l^{BOR}, \Delta\bar{\mathbf{q}}_{k*}^{ij})|) < tolerance$ **then**
Add neighbor j to set C
compute trial beta orientations $\beta_{m=j,l} = \bar{\mathbf{q}}^{D^{-1}} S_l^{\alpha} \bar{\mathbf{q}}^j$
end if
end for
if There are more than 3 unique variants in set C **then**
Calculate the parent β orientation: $\boldsymbol{\beta}_i = \min_{\boldsymbol{\beta}_i} \sum_{m=1}^{nNeighbors} (\boldsymbol{\beta}_i - \beta_{ml})^2 * I_{ml}\ S.T.\ I_{ml} \in \mathbb{Z}[0,1]\ ,\ \sum_{l=1}^{6} I_{ml} = 1\ \forall\ m$
add $\boldsymbol{\beta}_i$ to set B, to define the β orientation of α_i
remove α_i from set A
for j in set C **do**
Set $\boldsymbol{\beta}_i = \boldsymbol{\beta}_j$
Add $\boldsymbol{\beta}_j$ to set B
remove α_j from set A
end for
else
for j neighbors C **do**
if j already belongs to a β grain: $\beta_j \in B$ **then**
add α_i to the same β grain as its neighbor j
set $\boldsymbol{\beta}_i = \boldsymbol{\beta}_j$
Add $\boldsymbol{\beta}_i$ to set B
remove α_i from A
end if
end for
end if
end for
end while

Appendix B. Calibrated crystal plasticity parameters

Table 5
Porosity evolution parameters calibrated in Yang and Ghosh (2022). Here (T) and (C) refer to tension and compression.

Slip family	Equation	a	b		d	
			T	C	T	C
Basal	w_1	0.58	0.397	−0.114	78.703	38.985
	w_2	2.558	0.964	−0.781	105.892	60.664
	w_3	8.391				
	w_4				6.821	25.356
Prismatic $\langle a \rangle$ Pyramidal	w_1	1.191	0.135	0.188	270253	53.251
	w_2	1.079	0.363	0.228	−0.404	0.744
	w_3	0.005				
	w_4				−0.158	4.785
I+II $\langle c+a \rangle$ Pyramidal	w_1	1.187	0.599	0.188	0.335	1.604
	w_2	2.479	0.013	0.154	28.641	12.312
	w_3	6.189				
	w_4				2.370	1.743

Table 6
Slip system dependent parameters.

Parameter	Basal	Prismatic	$\langle a \rangle$ Pyramidal	I+II $\langle c+a \rangle$ Pyramidal
θ_{ref}	300 °K	300 °K	300 °K	300 °K
$\hat{\theta}_{ref}$	400 °K	200 °K	200 °K	160 °K
$\hat{g}$	176.58 MPa	132.43 MPa	132.43 MPa	353 MPa
h_0	150 MPa	150 MPa	150 MPa	150 MPa
$\widetilde{g}$	470 MPa	570 MPa	570 MPa	1550 MPa
c_1	0.08	0.062	0.07	0.05
c_2	1	1	1	1

The interaction matrices between slip systems are given by the following parameters: $\widetilde{q}^{\alpha\beta} = 1$, $\chi_{AF}^{\alpha\beta} = 1$, and $\chi_{AP}^{\alpha\beta} = 1$ for all slip system pairs.

Table 7
Components of the anisotropic elasticity tensor $\mathbb{C}$, expressed in Voigt notation, calibrated in Deka et al. (2006), with all other components being 0.

$\mathbb{C}_{11}, \mathbb{C}_{22}$	170.0 GPa
$\mathbb{C}_{33}$	204 GPa
$\mathbb{C}_{12}$	98 GPa
$\mathbb{C}_{23}, \mathbb{C}_{13}$	86 GPa
$\mathbb{C}_{44}$	36 GPa
$\mathbb{C}_{55}, \mathbb{C}_{66}$	51 GPa

Table 8
Additional material constants.

Parameter	Value
K	.162 $\frac{\text{MPa}}{\text{m}^{0.5}}$
G	48 GPa
Q	2.5^{-19} J
c	500 MPa
d	100

Appendix C. Quaternion notation

Relevant definitions are given below.

- • *Quaternion* $\bar{\mathbf{q}}$ contains a scalar component q_0 and a vector component $\mathbf{q}$.
- • *Superscripts* are used to define which grain or lath the quaternion represents.
- • $\Delta\bar{\mathbf{q}}^{ab}$ denotes the misorientation between two quaternions $\bar{\mathbf{q}}^a$ and $\bar{\mathbf{q}}^b$.
- • $\bar{\mathbf{q}}_{\mathbf{measured}}$ denotes the as measured orientation.
- • $\bar{\mathbf{q}} = \bar{\mathbf{q}}_{measured}[S_k^{HCP}]$ represents quaternions without the "measured" subscript, which denotes the quaternion after transformation to the fundamental zone.
- • *Subscript k* refers to a quaternion after the kth symmetry operator has been applied to it.
- • *Asterisk* k^* denotes a particular symmetry operator that satisfies or minimizes some operation, such as a transformation to the fundamental zone.

References

Anahid, M., Samal, M., Ghosh, S., 2011. Dwell fatigue crack nucleation model based on crystal plasticity finite element simulations of polycrystalline titanium alloys. J. Mech. Phys. Solids 59 (10), 2157–2176.

Ashby, M., 1970. The deformation of plastically non-homogeneous materials. Phil. Mag.: J. Theor. Exper. Appl. Phys. 21 (170), 399–424.

ASTM, 2011a. Standard test methods for tension testing of metallic materials E8/E8m. ASTM Stand. 3, 66.

ASTM, 2011b. Standard specification for titanium and titanium alloy bars and billets C348. ASTM Stand.: Nonferrous Met. Stand. Nonferrous Alloy Stand..

Azhari, F., Wallbrink, C., Sterjovski, Z., Crawford, B.R., Menzel, A., Agiu, D., Wang, C.H., Schaffer, G., 2022. Predicting the complete tensile properties of additively manufactured Ti-6Al-4V by integrating three-dimensional microstructure statistics with a crystal plasticity model. Int. J. Plast. 148, 103127.

Bagri, A., Weber, G., Stinville, J.-C., Lenthe, W., Pollock, T., Woodward, C., Ghosh, S., 2018. Microstructure and property-based statistically equivalent representative volume elements for polycrystalline Ni-based superalloys containing annealing twins. Metal. Mater. Trans. A 49 (11), 5727–5744.

Bailey, T., Stern, R., 2021. Instat. https://www.graphpad.com/scientific-software/instat/.

Benzing, J., Hrabe, N., Quinn, T., White, R., Rentz, R., Ahlfors, M., 2019. Hot isostatic pressing (HIP) to achieve isotropic microstructure and retain as-built strength in an additive manufacturing titanium alloy (Ti-6Al-4V). Mater. Lett. 257, 126690.

Benzing, J.T., Liew, L.-A., Hrabe, N., DelRio, F.W., 2020. Tracking defects and microstructural heterogeneities in meso-scale tensile specimens excised from additively manufactured parts. Experiment. Math. 60 (2), 165–170.

Beretta, S., Romano, S., 2017. A comparison of fatigue strength sensitivity to defects for materials manufactured by AM or traditional processes. Int. J. Fatigue 94, 178–191.

Bhattacharyya, D., Viswanathan, G., Denkenberger, R., Furrer, D., Fraser, H.L., 2003. The role of crystallographic and geometrical relationships between α and β phases in an α/β titanium alloy. Acta Mater. 51 (16), 4679–4691.

Bonatti, C., Mohr, D., 2017. Large deformation response of additively-manufactured fcc metamaterials: From octet truss lattices towards continuous shell mesostructures. Int. J. Plast. 92, 122–147.

Book, T.A., Sangid, M.D., 2016. Strain localization in Ti-6Al-4V Widmanstätten microstructures produced by additive manufacturing. Mater. Charact. 122, 104–112.

Boyce, B., Salzbrenner, B., Rodelas, J., Roach, A., Swiler, L., Madison, J., Jared, B., Shen, Y.-L., 2017. Extreme value statistics reveal rare failure-critical defects in additive manufacturing. Adv. Engin. Mater. 19 (8), 1700102.

Burgers, W., 1934. On the process of transition of the cubic-body-centered modification into the hexagonal-close-packed modification of zirconium. Physica 1 (7–12), 561–586.

Cayron, C., 2007. GenOVa: a computer program to generate orientational variants. J. Appl. Crystallogr. 40 (6), 1179–1182.

Chatterjee, K., Echlin, M.P., Kasemer, M., Callahan, P.G., Pollock, T.M., Dawson, P., 2018. Prediction of tensile stiffness and strength of Ti-6Al-4V using instantiated volume elements and crystal plasticity. Acta Mater. 157, 21–32.

Chen, W., Li, Z., 2019. Additive manufacturing of titanium aluminides. In: Froes, F., Boyer, B. (Eds.), Additive Manufacturing for the Aerospace Industry. Elsevier, pp. 235–263.

Cho, J.-H., Rollett, A., Oh, K., 2005. Determination of a mean orientation in electron backscatter diffraction measurements. Metall. Mater. Trans. A 36 (12), 3427–3438.
DeBotton, G., Castañeda, P., 1995. Variational estimates for the creep behaviour of polycrystals. Proc. Royal Soc. London. Series A: Math. Phys. Sciences 448, 121–142.
Deka, D., Joseph, D.S., Ghosh, S., Mills, M.J., 2006. Crystal plasticity modeling of deformation and creep in polycrystalline Ti-6242. Metall. Mater. Trans. A 37 (5), 1371–1388.
Dodge, Y., 2008. The Concise Encyclopedia of Statistics. Springer Science & Business Media.
Echlin, M.P., Mottura, A., Torbet, C.J., Pollock, T.M., 2012. A new TriBeam system for three-dimensional multimodal materials analysis. Rev. Sci. Instrum. 83 (2), 023701.
Feng, B., Bronkhorst, C.A., Liu, Z., Morrow, B.M., Cerreta, E., Li, W., Daphalapurkar, N., 2020. Three-dimensional modeling and simulations of single-crystal and bi-crystal titanium for high-strain-rate loading conditions. Int. J. Plast. 133, 102771.
Francois, M.M., Sun, A., King, W.E., Henson, N.J., Tourret, D., Bronkhorst, C.A., Carlson, N.N., Newman, C.K., Haut, T.S., Bakosi, J., Gibbs, J.W., Livescu, V., Vander Wiel, S.A., Clarke, A.J., Schraad, M.W., Blacker, T., Lim, H., Rodgers, T., Owen, S., Abdeljawad, F., Madison, J., Anderson, A.T., Fattebert, J.L., Ferencz, N.E., Khairallah, S.A., Walton, O., 2017. Modeling of additive manufacturing processes for metals: Challenges and opportunities. Curr. Opin. Solid State Mater. Sci. 21 (4), 198–206.
Frederick, C., Armstrong, P.J., 2007. A Mathematical Representation of the Multiaxial Bauschinger Effect, Vol. 24. Central Electricity Generating Board and Berkeley Nuclear Laboratories, pp. 1–26.
Gil, F., Ginebra, M., Manero, J., Planell, J., 2001. Formation of α-widmanstätten structure: effects of grain size and cooling rate on the widmanstätten morphologies and on the mechanical properties in Ti-6Al-4V alloy. J. Alloys Compd. 329 (1–2), 142–152.
Glavicic, M., Kobryn, P., Bieler, T., Semiatin, S., 2003a. An automated method to determine the orientation of the high-temperature beta phase from measured EBSD data for the low-temperature alpha-phase in Ti-6Al-4V. Mater. Sci. Engin.: A 351 (1–2), 258–264.
Glavicic, M., Kobryn, P., Bieler, T., Semiatin, S., 2003b. A method to determine the orientation of the high-temperature beta phase from measured EBSD data for the low-temperature alpha phase in ti-6al-4V. Mater. Sci. Engin.: A 346 (1–2), 50–59.
Gong, H., Rafi, K., Gu, H., Starr, T., Stucker, B., 2014. Analysis of defect generation in Ti–6Al–4V parts made using powder bed fusion additive manufacturing processes. Addit. Manuf. 1, 87–98.
Groeber, M.A., Jackson, M.A., 2014. DREAM. 3D: a digital representation environment for the analysis of microstructure in 3D. Int. Mater. Manuf. Innov. 3 (1), 56–72.
Han, X., Besson, J., Forest, S., Tanguy, B., Bugat, S., 2013. A yield function for single crystals containing voids. Int. J. Solids Struct. 50, 2115–2131.
Hu, D., Pan, J., Mao, J., Guo, X., Ji, H., Wang, R., 2020. An anisotropic mesoscale model of fatigue failure in a titanium alloy containing duplex microstructure and hard α inclusions. Mater. Des. 193, 108844.
Humbert, M., Gey, N., 2002. The calculation of a parent grain orientation from inherited variants for approximate (bcc–hcp) orientation relations. J. Appl. Crystall. 35 (4), 401–405.
Humbert, M., Wagner, F., Moustahfid, H., Esling, C., 1995. Determination of the orientation of a parent β grain from the orientations of the inherited α plates in the phase transformation from body-centred cubic to hexagonal close packed. J. Appl. Crystal. 28 (5), 571–576.
Kapoor, K., Yoo, Y.S.J., Book, T.A., Kacher, J.P., Sangid, M.D., 2018. Incorporating grain-level residual stresses and validating a crystal plasticity model of a two-phase Ti-6Al-4V alloy produced via additive manufacturing. J. Mech. Phys. Solids 121, 447–462.
Kasemer, M., Echlin, M.P., Stinville, J.C., Pollock, T.M., Dawson, P., 2017. On slip initiation in equiaxed α/β Ti-6Al-4V. Acta Mater. 136, 288–302.
Khairallah, S.A., Martin, A.A., Lee, J.R., Guss, G., Calta, N.P., Hammons, J.A., Nielsen, M.H., Chaput, K., Schwalbach, E., Shah, M.N., et al., 2020. Controlling interdependent meso-nanosecond dynamics and defect generation in metal 3D printing. Science 368 (6491), 660–665.
Knezevic, M., Ghorbanpour, S., Ferreri, N.C., Riyad, I.A., Kudzal, A.D., Paramore, J.D., Vogel, S.C., McWilliams, B.A., 2021. Thermo-hydrogen refinement of microstructure to improve mechanical properties of Ti-6Al-4V fabricated via laser powder bed fusion. Int. J. Plast. 809, 140980.
Kobryn, P., Semiatin, S.L., 2001. The laser additive manufacture of Ti-6Al-4V. J. Manage. 53 (9), 40–42.
Kocks, U.F., Tomé, C.N., Wenk, H.-R., 1998. Texture and Anisotropy: Preferred Orientations in Polycrystals and their Effect on Materials Properties. Cambridge University Press.
Krakow, R., Bennett, R.J., Johnstone, D.N., Vukmanovic, Z., Solano-Alvarez, W., Lainé, S.J., Einsle, J.F., Midgley, P.A., Rae, C.M., Hielscher, R., 2017. On three-dimensional misorientation spaces. Proc. R. Soc. Lond. A: Math. Phys. Eng. Sci. 473 (2206), 20170274.
Lin, Y., Tang, Y., Zhang, X.-Y., Chen, C., Yang, H., Zhou, K.-C., 2019. Effects of solution temperature and cooling rate on microstructure and micro-hardness of a hot compressed Ti-6Al-4V alloy. Vacuum 159, 191–199.
Ling, C., Besson, J., Forest, S., Tanguy, B., Latourte, F., Busso, E., 2016. An elastoviscoplastic model for porous single crystals at finite strains and its assessment based on unit cell simulations. Int. J. Plast. 84, 58–87.
Liu, S., Shin, Y.C., 2019. Additive manufacturing of Ti-6Al-4V alloy: A review. Mater. Des. 164, 107552.
Liu, P., Wang, Z., Xiao, Y., Lebensohn, R.A., Liu, Y., Horstemeyer, M.F., Cui, X., Chen, L., 2020. Integration of phase-field model and crystal plasticity for the prediction of process-structure-property relation of additively manufactured metallic materials. Int. J. Plast. 128, 102670.
Lütjering, G., Williams, J.C., 2007. Titanium. Springer Science & Business Media.
Mayeur, J., McDowell, D., 2007. A three-dimensional crystal plasticity model for duplex Ti–6Al–4V. Int. J. Plast. 23 (9), 1457–1485.
Mayeur, J.R., McDowell, D.L., Neu, R.W., 2008. Crystal plasticity simulations of fretting of Ti-6Al-4V in partial slip regime considering effects of texture. Comput. Mater. Sci. 41 (3), 356–365.
Montalbano, T., Briggs, B.N., Waterman, J.L., Nimer, S., Peitsch, C., Sopcisak, J., Trigg, D., Storck, S., 2021. Uncovering the coupled impact of defect morphology and microstructure on the tensile behavior of Ti-6Al-4V fabricated via laser powder bed fusion. J. Mater. Proc. Tech. 294, 117113.
MTEX, 2021. Fundamental regions. https://mtex-toolbox.github.io/OrientationFundamentalRegion.html. (Accessed 11 October 2021).
Muhammad, W., Brahme, A.P., Ibragimova, O., Kang, J., Inal, K., 2021. A machine learning framework to predict local strain distribution and the evolution of plastic anisotropy & fracture in additively manufactured alloys. Int. J. Plast. 136, 102867.
Ozturk, D., Pilchak, A., Ghosh, S., 2017. Experimentally validated dwell and cyclic fatigue crack nucleation model for α–titanium alloys. Scrip. Mater. 127, 15–18.
Ozturk, D., Shahba, A., Ghosh, S., 2016. Crystal plasticity FE study of the effect of thermo-mechanical loading on fatigue crack nucleation in titanium alloys. Fat. Fract. Engin. Mater. Struct. 39 (6), 752–769.
Pegues, J., Leung, K., Keshtgar, A., Airoldi, L., Apetre, N., Iyyer, N., Shamsaei, N., 2019. Effect of process parameter variation on microstructure and mechanical properties of additively manufactured Ti-6AL-4v. In: Solid Freeform Fabrication: Proc. 28th Annual Inter. Solid Freeform Fabrication Symposium – an Additive Manufacturing Conference. pp. 62–74.
Pinz, M., Weber, G., Lenthe, W., Uchic, M., Pollock, T., Ghosh, S., 2018. Microstructure and property based statistically equivalent RVEs for intragranular γ-γ'microstructures of Ni-based superalloys. Acta Mater. 157, 245–258.
Qiu, C., Adkins, N., Attallah, M., 2013. Microstructure and tensile properties of selectively laser-melted and of HIPed laser-melted Ti–6Al–4V. Mater. Sci. Eng. A 578, 230–239.
Radhakrishnan, B., Gorti, S., Babu, S.S., 2016. Phase field simulations of autocatalytic formation of alpha lamellar colonies in Ti-6Al-4V. Metall. Mater. Trans. A 47 (12), 6577–6592.

Salzbrenner, B., Rodelas, J., Shen, Y.-L., Madison, J., Jared, B., Swiler, L., Boyce, B., 2017. High-throughput stochastic tensile performance of additively manufactured stainless steel. J. Mater. Process. Technol. 241, 1–12.
Seifi, M., Salem, A., Beuth, J., Harrysson, O., Lewandowski, J.J., 2016. Overview of materials qualification needs for metal additive manufacturing. J. Manage. 68 (3), 747–764.
Shi, R., Wang, Y., 2013. Variant selection during α precipitation in Ti–6Al–4V under the influence of local stress: A simulation study. Acta Mater. 61 (16), 6006–6024.
Shi, R., Zhou, N., Niezgoda, S., Wang, Y., 2015. Microstructure and transformation texture evolution during α precipitation in polycrystalline α/β titanium alloys: A simulation study. Acta Mater. 94, 224–243.
Simmetrix Inc., 2015. Simulation modeling suite.
Thomas, J., Groeber, M.A., Ghosh, S., 2012. Image-based crystal plasticity FE analysis for microstructure dependent properties of Ti-6Al-4V alloys. Mater. Sci. Eng. A 553, 164–175.
Venkataramani, G., Kirane, K., Ghosh, S., 2008. Microstructural parameters affecting creep induced load shedding in Ti-6242 by a size dependent crystal plasticity FE model. Int. J. Plast. 24 (3), 428–454.
Venkatramani, G., Deka, D., Ghosh, S., 2006. Crystal plasticity based Fe model for understanding microstructural effects on creep and dwell fatigue in Ti-6242. J. Eng. Mater. Technol. 128 (3), 356–365.
Voisin, T., Calta, N.P., Khairallah, S.A., Forien, J.-B., Balogh, L., Cunningham, R.W., Rollett, A.D., Wang, Y.M., 2018. Defects-dictated tensile properties of selective laser melted Ti-6Al-4V. Mater. Des. 158, 113–126.
Watring, D.S., Benzing, J.T., Kafka, O.L., Liew, L.-A., Moser, N.H., Erickson, J., Hrabe, N., Spear, A.D., 2021. Evaluation of a modified void descriptor function to uniquely characterize pore networks and predict fracture-related properties in additively manufactured metals. Acta Mater. 117464.
Xu, Y., Fox, K., Rugg, D., Dunne, F., 2020. Cyclic plasticity and thermomechanical alleviation in titanium alloys. Int. J. Plast. 134, 102753.
Yang, Q., Ghosh, S., 2022. A crystal plasticity model for porous HCP single crystal titanium alloys under multiaxial loading conditions. Int. J. Solids Struct. 238, 111400.
Yang, Q., Zhang, P., Cheng, L., Min, Z., Chyu, M., To, A.C., 2016. Finite element modeling and validation of thermomechanical behavior of Ti-6Al-4V in directed energy deposition additive manufacturing. Addit. Manuf. 12, 169–177.
Zaitzeff, A., Pilchak, A., Berman, T., Allison, J., Esedoglu, S., 2021. A robust algorithm to calculate parent β grain shapes and orientations from α phase electron backscatter diffraction data in α/β-titanium alloys. Scrip. Mater. 191, 191–195.
Zhang, J., Li, X., Xu, D., Teng, C., Wang, H., Yang, L., Ju, H., Xu, H., Meng, Z., Ma, Y., et al., 2021. Phase field simulation of the stress-induced α microstructure in Ti–6Al–4 V alloy and its CPFEM properties evaluation. J. Mater. Sci. Technol. 90, 168–182.
Zheng, Z., Stapleton, A., Fox, K., Dunne, F., 2018. Understanding thermal alleviation in cold dwell fatigue in titanium alloys. Int. J. Plast. 111, 234–252.